1-1-2012

Orders of Magnitude Enhancement of Optical Nonlinear Phenomena in Subwavelength Metal-Dielectric Gratings

Daniel Ironside

WASHINGTON UNIVERSITY IN ST. LOUIS

School of Engineering and Applied Science

Department of Electrical and Systems Engineering

Thesis Examination Committee:
Jung-Tsung Shen, Chair
Lihong Wang
Barry Spielman

ORDERS OF MAGNITUDE ENHANCEMENT OF OPTICAL NONLINEAR PHENOMENA IN SUBWAVELENGTH METAL-DIELECTRIC GRATINGS

by

Daniel J. Ironside

A thesis presented to the School of Engineering
of Washington University in partial fulfillment of the
requirements for the degree of

MASTER OF SCIENCE

May 2012
Saint Louis, Missouri

ABSTRACT OF THE THESIS

Orders of Magnitude Enhancement of Optical Nonlinear Phenomena in Subwavelength Metal-Dielectric Gratings

by

Daniel J. Ironside

Master of Science in Electrical Engineering

Washington University in St. Louis, 2012

Research Advisor: Professor Jung-Tsung Shen

Nonlinear optical materials give rise to a multitude of phenomena that have important applications in technology and science. Due to small nonlinearities in naturally occurring materials, large optical fields are necessary to realize measurable nonlinear phenomena. The necessity of high intensity sources severely limits its use in practical applications, especially in low-powered devices. Several methods for enhancement of nonlinearity have been proposed, including use of conjugate polymers, resonators, and metallic nanoparticles. In this thesis, the nonlinear enhancement properties of subwavelength metal-dielectric gratings are explored. Enhancement in nonlinearity by several orders of magnitude is achieved, with the enhancement entirely controlled by the geometry of the structure, and independent of the wavelength of incident light. Ultimately, the nonlinear enhancement properties of metal-dielectric gratings allows for the reduction of input light intensity in producing nonlinear optical phenomena, and is an important step in the design low-powered nonlinear optical applications.

Acknowledgments

First and foremost, I offer gratitude to my research advicer, Dr. Jung-Tsung Shen, for the support and guidance thoughout my research at Washington University in St. Louis since 2010. He created a research environment for which I was able to explore many ideas without constraint. I have gained a wealth of knowledge and experience in science and engineering through his direction that is beyond value to my future endevour. For these things, I give many thanks.

I have many people to thank for fincanial support. First, I would like to give my thanks to Dr. Hiro Mukai, through which I received a NSF GK-12 Fellowship that enabled my continued education in engineering, and allowed me to stay in St. Louis while my wife studied medicine. Second, I would like to thank the National Science Foundation for the Graduate Research Fellowship award, which provided financial support for this thesis, and will continue support in my future studies.

During my time at Washington University in St. Louis, I receieved much assistance in the many fellowship and graduate school applications I submitted over the past few years. I would like to thank Dr. Jung-Tsung Shen, Dr. Goetz Bramesfeld, and Dr. Ian H. Redmount for providing timely letters of recommendation. Also, I would like to thank Sandra Matteucci in the engineering writing center to proofreading many application essays.

Finally, I would like to thank my wife, Abby, for all of the support and patience she has given me throughout all of studies. Also, I would like to thank my parents for providing and encouraging higher academic achievement.

Daniel J. Ironside

Washington University in Saint Louis
May 2012

Contents

List of Tables

List of Figures

Chapter 1

Thesis Introduction

1.1 Summary

Nonlinear optical materials give rise to a multitude of phenomena that have important applications in technology and science. One fundamental example is harmonic generation, in which light combines to form new light at integer multiples of the input frequency. Materials capable of harmonic generation are of practical importance since they are able to generate or detect light at frequencies that are not available in current optical devices. Another fundamental example is optical bistability, in which the intensity of output light can take two distinct stable values for a given input, creating an optical two-state system. Bistable devices, such as optical logic gates and memory, are critically important for optical computing, which promises much faster computation than in current electronic devices. The degree of optical nonlinearity in a material depends upon the strength of the optical field, and varies in different materials. Due to very small nonlinearities in naturally occurring materials, large optical fields are necessary to realize measurable nonlinear phenomena. The necessity of high intensity sources to observe the effects of optical nonlinearity severely limits it use in practical applications, especially in low-powered devices. To realized such devices, the enhancement of nonlinear material properties is required. Several methods for enhancement of nonlinearity have been proposed, including use of quantum wells, Fabry-Perot resonators, and metallic nanoparticles. Recently, there has been interest in characterizing the optical response of subwavelength metallic structures containing nonlinear dielectric materials. Examples include subwavelength metallic gratings, [1, 2, 3], and hole arrays [4]. In this thesis, the nonlinear enhancement

properties of subwavelength metal-dielectric gratings are explored. Through several numerical calculations, enhancement in nonlinearity by several orders of magnitude is achievable in subwavelength metal-dielectric gratings. Also, a general scaled mapping from the far-field nonlinear optical response of the grating to a homogeneous dielectric slab with enhanced nonlinearity is derived. In validation, the enhancement is demonstrated in harmonic generation and optical bistability for common nonlinear dielectric materials. By this method, the enhancement in metal-dielectric gratings is entirely controlled by the geometry of the structure, and independent of the wavelength of incident light. Ultimately, the nonlinear enhancement properties of metal-dielectric gratings allows for the reduction of input light intensity in producing nonlinear optical phenomena. More specifically, the grating is an important step in the design of low-powered nonlinear optical applications.

1.2 Thesis Outline

Chapter 2 is a brief introduction to nonlinear optics. Topics covered are nonlinear material definitions for second and third order nonlinearity as well as nonlinear optical phenomena focusing on harmonic generation and optical bistability.

Chapter 3 is a brief overview of nonlinear enhancement techniques from scientific and engineering literature. Focus is given to microscopic enhancement techniques of hyperpolarization of conjugate polymers and quantum wells as well as macroscopic techniques of metallic nanoparticles, resonators, and subwavelength metallic gratings.

Chapter 4 is the quantification of nonlinear enhancement of metal-dielectric gratings at subwavelength scales. Here, physical arguments are developed for nonlinear enhancement. Also, simple and general scaled mappings are derived.

Chapter 5 is the verification of nonlinear enhancement of metal-dielectric gratings at subwavelength scales. Many orders of magnitude enhancement is demonstrated in second and third harmonic generation and optical bistability.

Appendix A is a brief introduction to the finite difference method and FDTD for electrodynamic systems. Also, boundary conditions for FDTD simulation are discussed.

Appendix B is the computational summary and validation for FDTD simulation of both nonlinear homogeneous dielectric slabs and nonlinear subwavelength metal-dielectric gratings. Error analysis and convergence is discussed.

Chapter 2

Introduction of Nonlinear Optics

Nonlinear optics is a field of optics that describes the changes of the optical properties of materials in the presence of light. This behavior is contrary to everyday experience, but is firmly rooted in the interaction of light with matter at atomic scales. Effects resulting from nonlinear optics arises from light at large intensities within materials. These nonlinear properties produce a plethora of interesting phenomena such as wave mixing and bistability. In this chapter, a basic introduction to nonlinear optics is provided. Nonlinear optics is a rich field that provides many useful applications in fundamental science and technology; however, focus is given on optical materials and phenomena directly related to content of this thesis.

2.1 General Nonlinear Optical Theory

Throughout the field of Optics, many materials have optical properties that are dependent upon "what" and "how" light is present within the medium. For example, many materials have dispersive properties; when glass is shaped as a prism, white light becomes separated through dispersion, and results in an index of refraction that is frequency dependent. Another example is materials with birefringence which results in an incidence dependent index of refraction for same frequencies of light. Thus, through covering the whole of Optics, it should be of no surprise to find that optical materials can have properties that are electric field dependent. It is through this field dependence that materials are known to have optical nonlinearity.

The physical picture of optical nonlinearity in materials starts with the permittivity of materials. Under typical conditions, optical material have a linear relation between polarization density, $\mathbf{P}$, and electric field, $\mathbf{E}$ as

$$\mathbf{P} = \epsilon_\mathbf{0}\epsilon_\mathbf{l}\mathbf{E} \tag{2.1}$$

where ϵ_0 is the permittivity of free space and ϵ_l is the permittivity of the material. In the presence of light, the ratio of the speed of light in free space to the speed of light in the material, known as the index of refraction, n, is directly related to the permittivity of the material as

$$n = \sqrt{\epsilon_l \mu_l} \tag{2.2}$$

where μ_l is the permeability of the material. For non-magnetic materials and dielectric materials by definition, $\mu_l = 1$. Thus, $n = \sqrt{\epsilon_l}$

The permittivity of a material under the linear relation between electric field and polarization density works well under most optical conditions, such as waveguiding in optical fibers. However, when the electric field become very large, the linearity condition no longer holds. The source of optical nonlinearity is found at the atomic level. The electric field that binds the electron to the nucleus of an atom is very larger, on the order of 10^{11}. When an external electric field is applied to the atom via light, under normal conditions, its field perturbation on the electron is very small, causing little effect to the atomic polarization. This justifies the linearity of the polarization density relation. However, increasing the field intensity of light to atomic levels within the material results in a great perturbation of the electron beyond the linear limit. This results in nonlinear effects and invalidates the linear polarization density relation.

Mathematically, the polarization density relation with the electric field can be generalized through a Taylor series expansion.

$$\mathbf{P} = \epsilon_\mathbf{0}(\epsilon_\mathbf{l}\mathbf{E} + \chi^{(\mathbf{2})}|\mathbf{E}|^\mathbf{2} + \chi^{(\mathbf{3})}|\mathbf{E}|^\mathbf{3} + \ldots) \tag{2.3}$$

For small electric fields, only the first term is kept. This gives the linear relation as discussed. However, if the electric field is large enough, the higher-order terms must be kept. When this occurs, the polarization density is no longer linear, and becomes nonlinear. The second-order term is known as second-order nonlinearity with a second-order nonlinear coefficient $\chi^{(2)}$. Similarly, the third-order term is known as third-order nonlinearity with a third-order nonlinear coefficient $\chi^{(3)}$. More detailed information regarding these particular nonlinear terms in real materials can be found in the remaining sections in this Chapter. Higher order effects beyond the third-order are possible in theory, however, often are not observed in the lab due to extreme field requirements to realize them, and therefore will not be given treatment in this thesis.

This concludes the brief introduction to general nonlinear optical theory. From here, physical treatment is given to second-order and third-order nonlinear materials. Also, related nonlinear phenomena are discussed. For more information related to nonlinear optics, refer to [5].

2.2 Second-Order Nonlinear Optics

To expand upon the theory discussed above, a brief introduction to second-order nonlinear optics is given. In this section, a practical material definition for second-order nonlinear materials is determined. Also, common second-order nonlinear materials are listed and described. Lastly, optical phenomena produced by second-order nonlinearity are discussed. Particular attention is given to second harmonic generation, as it is the main phenomena discussed later in the thesis.

2.2.1 Second-Order Nonlinearity Definition

Materials with second-order nonlinearity display a polarization density describe by the first nonlinear term, where all other higher nonlinear terms are neglected.

$$\mathbf{P} = \epsilon_{\mathbf{0}}(\epsilon_{\mathbf{l}}\mathbf{E} + \chi^{(\mathbf{2})}|\mathbf{E}|^{\mathbf{2}}) \tag{2.4}$$

Although the polarization density description of second-order nonlinearity is technically correct, a more useful definition of second-order nonlinearity can be produced from it. Here, the goal is to have the second-order nonlinearity combined into one material permittivity definition. This is easily achieved by factoring out one electric field in the polarization density above.

$$\mathbf{P} = \epsilon_{\mathbf{0}}(\epsilon_{\mathbf{1}} + \chi^{(\mathbf{2})}|\mathbf{E}|)\mathbf{E} \tag{2.5}$$

Next, combine both the linear and second-order nonlinear parts into a total permittivity ϵ.

$$\mathbf{P} = \epsilon_{\mathbf{0}}\epsilon\mathbf{E} \tag{2.6}$$

Now, this looks like the linear definition, expect now the total permittivity is field dependent.

$$\epsilon = \epsilon_l + \chi^{(2)}|\mathbf{E}| \tag{2.7}$$

From the total permittivity definition of second-order nonlinearity, it is seen that the second-order nonlinear effect is specifically dependent upon the electric field within the material. Also, the linear part remains the same, so for small field inputs, the total permittivity is linear which is consistent with the previous linear theory.

2.2.2 Material Types

The key feature of second-order nonlinear materials is their crystalline structure breaks inversion symmetry, i.e. the properties of the crystal change by the transformation $\mathbf{r} \rightarrow -\mathbf{r}$. Materials with inversion symmetry cannot exhibit second-order nonlinearity, as the transformation eliminates the second-order term in the polarization density. However, materials with inversion symmetry exhibit third-order nonlinearity, which is discussed in the next section. Second-order nonlinear optical materials

occur in nature and are often used in scientific and engineering disciplines. As a reference to later happenings in this thesis, a collection of the most common second-order nonlinear materials are listed in Table 2.1. A complete lists of measured second-order nonlinear materials can be found here [6].

Second-Order NL Materials			
Material Name	$\lambda\ (\mu m)$	ϵ_l	$\chi^{(2)}\ (pm/V)$
Lithium niobate	1.058	4.98	0.84
Copper bromide	10.6	3.88	16.0
Copper chloride (I)	10.6	3.58	13.4
Gallium arsenide	10.6	11.5	150
Tellurium	10.6	22.96	1340
Cadmium selenide	10.6	5.98	108

Table 2.1: Linear and nonlinear optical properties of common second-order nonlinear materials in the near to mid infrared frequency range. Units in MKS

Although many second-order materials are listed over a wide range of wavelengths, attention is focused to second-order materials in the mid-infrared range. Specifically, the second-order nonlinear properties of Copper Chloride (I) (CuCl(I)) at 10.6 μm are used throughout this thesis.

2.2.3 Second Harmonic Generation

Second harmonic generation is a second order nonlinear optical process in which light at frequency ω combines to form new light at frequency 2ω. Second harmonic generation is unique to second-order nonlinear materials, as seen in Figure 2.1.

Here, light at frequency ω is pumped into a second-order nonlinear crystal and light with frequencies ω and 2ω are transmitted. Cleverly, a prism is used to separate the frequencies into two separate beams. Second harmonic generation can occur with partial to full conversion from the input. In general, the second harmonic conversion efficiency is

$$\eta_{SHG} = \frac{4\left(\chi^{(2)}\right)^2 \omega^2 L^2 I}{n^3 c^3 \epsilon_0} \tag{2.8}$$

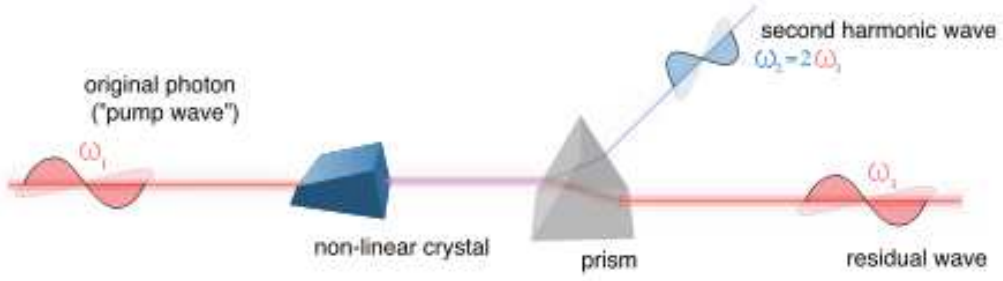

Figure 2.1: Shown is a simple experimental setup for creation of second harmonic generation from second-order nonlinear materials. Light at frequency ω is pumped into a second-order nonlinear crystal and light with frequencies ω and 2ω are transmitted. A prism is used to separate the frequencies into two separate beams.

where L is the slab thickness and I is the intensity. Thus, for full conversion, a suitable long slab in necessary at low intensities. Energy conservation consideration dictate that for full conversion, the second harmonic light is at half the intensity of the input, as two input photons combined to form one output photon.

In general, second harmonic generation is a special type of second-order nonlinear phenomena of three wave mixing. Here, light a two different frequencies ω_1 and ω_2 can add or subtract to form new light. Specifically, second harmonic generation is three wave mixing addition where $\omega_1 = \omega_2 = \omega_{input}$.

Lastly, full conversion requires perfect or quasi phase matching between the input frequency and corresponding second harmonic. For simple systems, the index of refraction at the input frequency must match the index of refraction of the second harmonic for ideal conditions. In most materials, this does not occur due to dispersion. To overcome this, many techniques have been created, such as periodic poling [7], for near perfect phase matching conditions.

2.3 Third-Order Nonlinear Optics

2.3.1 Third-Order Nonlinearity

Materials with third-order nonlinearity display a polarization density describe by the second nonlinear term, where the first and all other higher nonlinear terms are neglected. The first nonlinear term is neglected specifically because material exhibiting second-order nonlinearity do not have inversion symmetry. Here, materials that do have inversion symmetry lose the first nonlinear term, leaving the second nonlinear term, as seen below.

$$\mathbf{P} = \epsilon_{\mathbf{0}}(\epsilon_{\mathbf{l}}\mathbf{E} + \chi^{(\mathbf{3})}|\mathbf{E}|^{\mathbf{3}}) \tag{2.9}$$

Although the polarization density description of third-order nonlinearity is technically correct, a more useful definition of third-order nonlinearity can be produced from it. Here, the goal is to have the third-order nonlinearity combined into one material permittivity definition. This is easily achieved by factoring out one electric field in the polarization density above.

$$\mathbf{P} = \epsilon_{\mathbf{0}}(\epsilon_{\mathbf{l}} + \chi^{(\mathbf{3})}|\mathbf{E}|^{\mathbf{2}})\mathbf{E} \tag{2.10}$$

Next, combined both the linear and third-order nonlinear parts into a total permittivity ϵ.

$$\mathbf{P} = \epsilon_{\mathbf{0}}\epsilon\mathbf{E} \tag{2.11}$$

Now, this looks like the linear definition, expect now the total permittivity is field dependent.

$$\epsilon = \epsilon_l + \chi^{(3)}|\mathbf{E}|^{\mathbf{2}} \tag{2.12}$$

From the total permittivity definition of third-order nonlinearity, it is seen that the third-order nonlinear effect is specifically dependent upon the electric field squared within the material; this can also be thought as the intensity within the nonlinear medium. Also, the linear part remains the same, so for small field inputs, the total permittivity is linear which is consistent with linear theory.

2.3.2 Material Types

The key feature of third-order nonlinear materials is their crystalline structure does not break inversion symmetry, i.e. the properties of the crystal do not change by the transformation $\mathbf{r} \rightarrow -\mathbf{r}$. Materials with inversion symmetry cannot exhibit second-order nonlinearity, as the transformation eliminates the second-order term in the polarization density. However, materials without inversion symmetry can exhibit second-order nonlinearity, which is discussed in the previous section. Third-order nonlinear optical materials occur in nature and are often used in scientific and engineering disciplines. As a reference to later happenings in this thesis, a collection of the most common third-order nonlinear materials are listed in Table 2.2. A complete lists of measured third-order nonlinear materials can be found here [6].

Third-Order NL Materials			
Material Name	$\lambda\ (\mu m)$	ϵ_l	$\chi^{(3)}\ (m^2/V^2)$
Silica (I)	1.064	2.25	8e-23
Gallium arsenide	10.6	10.89	1.49e-19
Silicon	10.6	11.56	7.4e-20
Germanium	10.6	16	1.05e-19

Table 2.2: Linear and nonlinear optical properties of common third-order nonlinear materials in the near to mid infrared frequency range. Units are in MKS.

Although many third-order materials are listed over a wide range of wavelengths, attention is focused to third-order materials in the mid-infrared range. Specifically, the third-order nonlinear properties of Gallium Arsenide (GaAs) and Silicon (Si) at 10.6 μm are used throughout this thesis.

2.3.3 Optical Kerr-Effect

The optical Kerr effect is special to third-order nonlinear materials. Because of the symmetry in its nonlinear permittivity, it can be expressed as an intensity dependent index of refraction for small input intensities. This formulation is useful in measurement of $\chi^{(3)}$ in materials and for physical understanding of third-order nonlinear effects in transmission spectra and optical bistability.

The derivation is rooted in the linear index of refraction as the square root of the relative permittivity

$$n = \sqrt{\epsilon} \tag{2.13}$$

With constant relative permittivity in linear optical systems, the index of refraction is also constant. However, the permittivity definition of third-order nonlinear systems is dependent upon the square of the electric field within the material

$$\epsilon = \epsilon_l + \chi^{(3)}|\mathbf{E}|^{\mathbf{2}} \tag{2.14}$$

Applying the same approach as in the index of refraction, it is expected that the third-order nonlinear index of refraction is field dependent as well. Thus, taking the square root

$$n_{nonlinear} = \sqrt{\epsilon_l + \chi^{(3)}|\mathbf{E}|^{\mathbf{2}}} \tag{2.15}$$

However, this is rather cumbersome in this form, so it is assumed that the third-order nonlinear material experiences small electric fields. Thus, by factoring the linear permittivity out of the square root, and applying the binomial expansion

$$n_{nonlinear} = \sqrt{\epsilon_l}(1 + \frac{\chi^{(3)}}{2\epsilon_l}|\mathbf{E}|^{\mathbf{2}}) \tag{2.16}$$

Since $n_0 = \sqrt{\epsilon_l}$, the nonlinear index of refraction becomes

$$n_{nonlinear} = n_0 + \frac{\chi^{(3)}}{2n_0}|\mathbf{E}|^{\mathbf{2}} \tag{2.17}$$

Using the definition of intensity as

$$I = \frac{1}{2}c\epsilon_0|\mathbf{E}|^{\mathbf{2}} \tag{2.18}$$

the nonlinear index of refraction becomes

$$n(I) = n_0 + \frac{\chi^{(3)}}{c\epsilon_0 n_0^2} I \tag{2.19}$$

Defining a nonlinear index of refraction coefficient as

$$n_2 = \frac{\chi^{(3)}}{c\epsilon_0 n_0^2} \tag{2.20}$$

the final form of the nonlinear index of refraction via the optical Kerr effect is

$$n(I) = n_0 + n_2 I \tag{2.21}$$

Thus, for small input intensity into third-order nonlinear materials, the index of refraction of the material changes linearly. As long as the product of $n_2 I$ remains sufficiently small, this definition of third-order optical nonlinearity can be applied to experiment where n_2 is measured, from which $\chi^{(3)}$ can be found, or it can be used in theoretical calculation of interesting nonlinear phenomena, such as optical bistability, when intensity inputs are weak overall.

2.3.4 Third Harmonic Generation

Third harmonic generation is a third-order nonlinear optical process in which light at frequency ω combines to form new light frequency 3ω. Third harmonic generation is unique to third-order nonlinear materials, as seen in Figure 2.2.

Here, light at frequency ω is pumped into a third-order nonlinear crystal and light with frequencies ω and 3ω are transmitted. Cleverly, a prism is used to separate the frequencies into two separate beams.

Third harmonic generation can occur with partial to full conversion from the input. Energy conservation consideration dictate that for full conversion, the third harmonic light is at a third the intensity of the input, as three input photons combined to form one output harmonic photon.

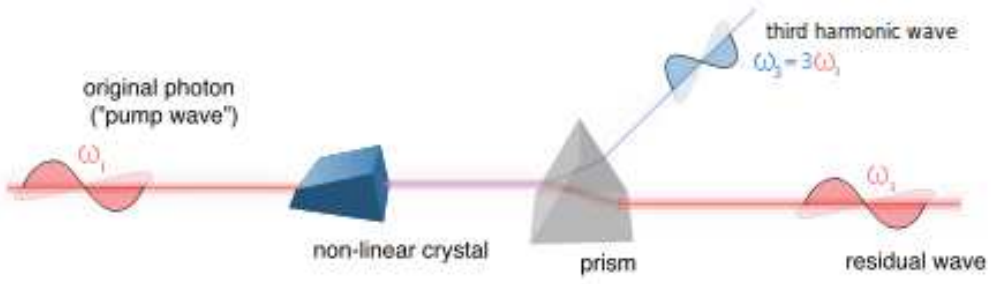

Figure 2.2: Shown is a simple experimental setup for creation of third harmonic generation from third-order nonlinear materials. Light at frequency ω is pumped into a third-order nonlinear crystal and light with frequencies ω and 3ω are transmitted. A prism is used to separate the frequencies into two separate beams.

In general, third harmonic generation is a special type of third-order nonlinear phenomena of four wave mixing. Here, light a three different frequencies ω_1, ω_2, and ω_3 can add or subtract to form new light. Specifically, third harmonic generation is three wave mixing addition where $\omega_1 = \omega_2 = \omega_3 = \omega_{input}$.

2.3.5 Optical Bistability

Optical bistability is a third-order nonlinear process by which light can have two possible transmitted intensity states at one input intensity, as seen in Figure 2.3.

The graph of optical bistability forms a hysteresis curve. Outside the two-state region, output light takes one stable value. Within the two-state region, there exists an upper state and a lower state. These two-states are stable; however, how they are reached is dependent where the previous single valued transmission state was located. To reach the lower state, light must start in the single-valued lower state branch, and through increasing the intensity, the lower state can be reached. Similarly, to reach the upper state, light must start in the single-valued upper state branch, and through decreasing the intensity, the upper state can be reached. In effect, the memory of previous location in the nonlinear system yields the upper or lower state branches. More information on optical bistability can be found here [8].

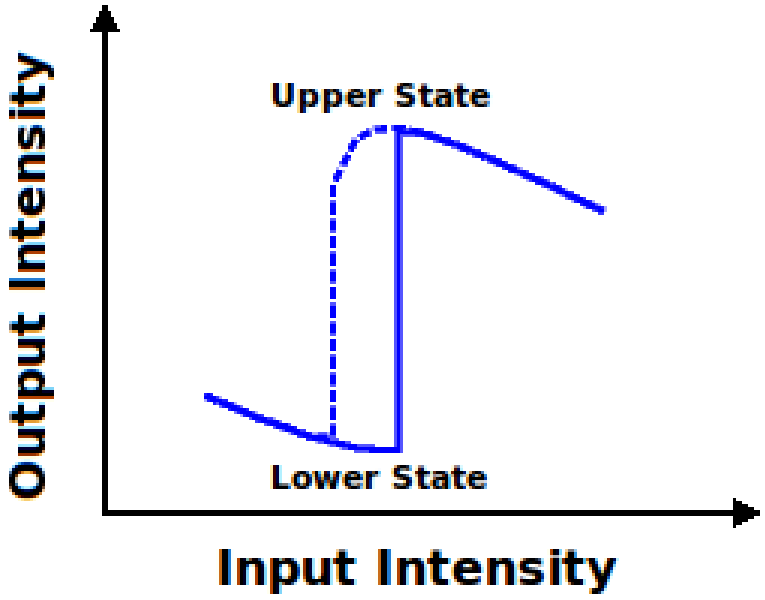

Figure 2.3: Shown is the hysteresis curve for a third-order nonlinear material in optical bistability. Nonlinear system exhibiting optical bistability have two stable transmission states for a single input intensity. The upper state is arrived from higher intensities above the hysteresis. The lower state is arrived from the lower intensities below the hysteresis.

Chapter 3

Techniques for Nonlinear Optical Enhancement

Nonlinear optical materials have many interesting phenomena that have potential use in optical devices and technology. However, in there current state, nonlinear optical materials produce very weak nonlinear optical responses, requiring large laser intensity to realize nonlinear phenomena. This trait lead nonlinear optical materials to be impractical, especially in low powered optical devices, and too bulky for on-chip integration. Thus, in order for nonlinear optics to enter the practical regime, the overall nonlinearity must be enhanced. In this Chapter, physical considerations for nonlinear enhancement are discusses, and current nonlinear enhancement techniques are categorized.

3.1 Physical Considerations

The primary limitation of nonlinear optics in practical applications is the relatively weak response of optical nonlinearity in natural occurring materials. For applications of nonlinear optical phenomena to be used in realistic devices, the overall optical nonlinearity of materials must be significantly enhanced by many orders of magnitude. In this section, the weak nature of nonlinear optical materials is described, and pathways for nonlinear enhancement are suggested.

3.1.1 Nonlinear Optical Limitations

As discussed in Chapter 1, nonlinear optics provides a plethora of optical phenomena, such as optical bistability and frequency mixing, that have distinct scientific interest, and also important applications to optical devices. For example, the hysteresis of optical bistability in third-order nonlinear materials can be utilized to create the two-state logic systems needed for optical gates and memory [9, 10, 11]. This optical logic is of critical importance to all-optical computing, which promises much faster computation than current electronic methods. Also, optical computing eliminates the need for optical-to-electronic and electronic-to optical transitions for computing purposes in optical devices, such as long distance fiber optics communications. Another important example is the utilization frequency mixing within second and third-order nonlinear materials. Under suitable conditions, these materials can generate or detect light at frequencies that are not currently available in lasers or detectors [12, 13, 14]. This has a particular importance to research in THz light sources and detectors, which has great application to biological and chemical measurement as well as medical imaging, but is severely lacking in the current available technology catalog, [15, 16, 17]. Just from these examples, it is clear that nonlinear optical materials can play an important role is the design of many emerging optical devices and technologies.

However, even with the many great properties of nonlinear optical materials, they have many undesirable qualities that severely limit its use in practical applications and devices utilizing nonlinear optical phenomena. The source of practical limitation in naturally occurring nonlinear optical materials is its inherit weak nonlinearity, in particular, $\chi^{(2)}$ and $\chi^{(3)}$. Going back to the permittivity definition of optical nonlinearity, the total nonlinear effect is dependent upon the nonlinear coefficient, $\chi^{(2)}$ for second-order materials and $\chi^{(3)}$ for third-order materials, and the field present within the material, $|E|$ for second-order materials and $|E|^2$ for third-order materials as seen below. Thus, the total nonlinear effect on the material is based on the product of the nonlinear coefficient and the field present within the material. Given this property, to yield strong nonlinear effects given a small nonlinear coefficient requires a large field input, on the order of $10^{16} W/cm^2$ [18].

Using the bulk nonlinearity properties of naturally occurring materials becomes impractical for all-optical commercial devices. The first drawback is the high intensities

needed to generate nonlinear optical phenomena within the device. High intensity laser sources are in general large, and cannot be scaled down for chip sized integration. Also, even with small scale, high intensity sources in place, high intensities require large powers, which are also impractical for commercial devices relying on low-power requirements. Furthermore, for length dependent nonlinear optical processes, the length scales necessary are in general in the centimeter scales, much larger than the micro scale needed for on-chip integration. Thus, for nonlinear optics to be used in practical applications at chip scale and at low powers, enhancement of nonlinearity is necessary.

3.1.2 Pathways for Nonlinear Enhancement

From the field-dependent permittivity definition of optical nonlinear materials, it is clear there are two pathways for enhancement of nonlinearity. The first approach is the microscopic manipulation of materials that generate enhanced nonlinearity that do not occur in nature. From the microscopic approach, the goal is to yield an larger $\chi^{(2)}$ or $\chi^{(3)}$ in the nonlinear material of interest. For this to work, suitable modification of electronic, atomic, or molecular polarizations or quantum states is necessary in creation of new, enhanced nonlinear materials, not occurring in nature. The second approach is the macroscopic organization of materials in structures that generate enhanced nonlinearity. For the macroscopic approach, the goals is to yield a larger $|E|$ or $|E|^2$ within the nonlinear material of interest. For this to work, structures containing nonlinear materials must locally enhance the fields surrounding the nonlinear materials, producing an overall enhancement in optical nonlinearity using naturally occurring nonlinear materials.

3.2 Past Enhancement Techniques

Using the pathways for nonlinear enhancement, many different approaches in generating enhanced nonlinearity have been proposed in the literature. In this section, a

brief categorization of nonlinear enhancement techniques from the literature is provided. For each type, the nonlinear enhancement technique is described and nonlinear enhancement quantified.

3.2.1 Hyperpolarizability of Conjugated Polymers

Hyperpolarizability of Conjugate Polymers is a microscopic enhancement technique that generates enhanced optical nonlinearity through modification of the polarizability on conjugate polymers, which translates into larger second-order and third-order nonlinearities. This technique has been experimentally verified, and observed many orders of enhancement in second and third order nonlinearity within conjugate polymers [19, 20]. Although these microscopic enhancements yield many orders of magnitude enhancement, they only apply to conjugate polymer materials. Thus, when compared to other nonlinear materials, they only do marginally better than the naturally occurring nonlinearity in semiconductors.

3.2.2 Quantum Wells

Quantum Wells is a microscopic enhancement technique that generates enhanced optical nonlinearity through modification of semiconductor energy levels and energy sub-bands, which translates into larger second-order and third-order nonlinearities [21, 22, 23]. This technique has been theoretically discussed and experimentally verified with many orders of magnitude enhancement in optical bistability [24], and harmonic generation [25].

3.2.3 Plasmonic Nanoparticles

Plasmonic nanoparticles is a macroscopic enhancement technique that generates enhanced optical nonlinearity through local field enhancement from plasmonic responses of injected metallic nanoparticles into nonlinear materials. This technique has been theoretically discussed and experimentally verified with many orders of magnitude

enhancement in second order, and third order nonlinearity [26, 27, 28, 29]. Currently, one disadvantage of this approach is yielding a consistent injected placement and number of nanoparticles in a nonlinear material. This is particularly important as optical devices in mass production require consistent material properties in the manufacturing process.

3.2.4 Resonators

Resonators either containing nonlinear materials or are themselves nonlinear materials is a macroscopic enhancement technique that produces large nonlinear enhancement through strong confined local electric fields within cavities. One type of resonator is the nonlinear Fabry-Perot resonator which is simply two facing mirrors with a nonlinear material place between the mirrors. Incoming light is trapped between the mirrors, resulting in an enhanced local field between the mirrors, and as a result, large nonlinearity. This has been shown to be order of magnitude enhancement in optical bistability [30, 31], and order of magnitude enhancement in second harmonic generation [32]. Although nonlinear Fabry-Perot produces large enhancement, its main limitation is its bulky size, on the centimeter scales, which prohibits its use in on-chip integration for practical optical devices. Also, specifically in bistability cases, nonlinear Fabry-Perot has slow switching times, roughly 25 ps, which lowers the speed in optical computation or memory.

Another popular resonator enhancement technique is micro-ring resonators, which are spherical or toroid shaped optical materials, which light is coupled into where it is confined to through whispering gallery modes. Nonlinear enhancement has been observed in very low power optical bistability [33, 34], and efficient wave mixing [35, 36]. Micro-ring resonators have the beneficial size at micro scales; however, increasing the quality factor general increasing the switching times, which are not beneficial.

3.2.5 Subwavelength Metallic Apertures

Subwavelength metallic apertures containing nonlinear materials is a macroscopic enhancement technique that produces large nonlinear enhancement through strong confined local electric fields within the subwavelength metallic apertures. This technique has been theoretically and experimentally demonstrated for second and third order nonlinear materials in a number of nonlinear optical phenomena. Several orders of magnitude enhancement of optical bistability and optical switching were theoretically calculated in subwavelength metallic gratings with third order nonlinear materials [1, 3]. Similarly, in subwavelength metallic gratings, propagating solitons were calculated for third-order nonlinearity [2]. In subwavelength metallic hole arrays, one order of magnitude enhancement of second harmonic generation was experimentally verified [4].

This concludes the brief categorization nonlinear enhancement techniques. From here, the thesis specializes to nonlinear enhancement of subwavelength metallic apertures containing both second order and third order nonlinear dielectric materials in demonstration of enhancement harmonic generation and optical bistability.

Chapter 4

Characterization of Nonlinear Enhancement in Subwavelength Metal-Dielectric Gratings

In this chapter, the enhancement properties of metallic arrays containing nonlinear dielectric materials are discussed. The physical structure and field properties of metal-dielectric gratings at subwavelength scales are developed. Also, a simple scaled mapping between nonlinear metal-dielectric gratings and homogeneous nonlinear dielectric slabs is derived to quantify physical characteristics. Lastly, a general scaled mapping is proposed for a complete physical mapping that accurately predicts nonlinear phenomena.

4.1 Physical Systems of Subwavelength Metal Dielectric Gratings

Gratings have provided a means for exploring a multitude of phenomena in engineering and physics. From classical wave interference to the famous double slit experiment, gratings play a major role in classical and modern physics. However, in all of these applications, the role of gratings is to provide wave interference. More surprising are the properties of gratings above the diffraction limit, specifically when light is larger

than several slit lengths known as subwavelength. In this section, the grating structure and transmission properties of subwavelength gratings are described. Also, the local enhancement properties of metallic arrays are discussed.

4.1.1 Grating Layout and Assumptions

In the analysis of subwavelength metal-dielectric gratings, several important quantities of the system are defined in order to describe its structure and its field properties. A simple drawing of a metal-dielectric grating at subwavelength scales is shown in Figure 4.1. To begin, we set a coordinate system ideal for the analysis. The positive x-direction is set along the horizontal axis, pointing to the right. The positive z-direction is set pointing out of the figure. Lastly, the positive y-direction is set along the vertical axis, pointing down. The y-direction has an atypical pointing direction for convenience since input light travels from top to bottom in the numerical analysis.

In Figure 4.1, the basic layout of the metal-dielectric grating is shown. Here, metal (shown as black) and dielectric (shown as blue) materials are layered periodically in the x-direction. The periodicity length of the system, notated as d, describes the length in which layered metal and dielectric materials repeat in the grating. In this analysis, the grating is assumed to be infinite in the x-direction, and thus, has infinite periods. This assumption neglects grating end effects in the analysis. The slit width of the system, notated as a, describes the length between repeating metal layers. The slit width is also the width of the nonlinear dielectric layer in the grating. Lastly, the film thickness of the system, notated as L, in the thickness of the grating.

For reasons to be discussed in the remaining subsections, the transmission and nonlinear enhancement of metal-dielectric gratings depends on several assumptions, and are listed. (1) The wavelength of the incidence light is much greater in length than one periodicity of the metal-dielectric grating. This assumption is known as subwavelength scaling. (2) The light polarization is trans-magnetic polarized (of TM polarization) at the grating interface. Here, the electric field oscillation is always normal to the metallic slits. For trans-electric polarization of light, the metal-dielectric grating does not generate any transmission modes or field enhancement effects due to electric field evanescence in the slits. Because of this, the analysis of gratings at TE

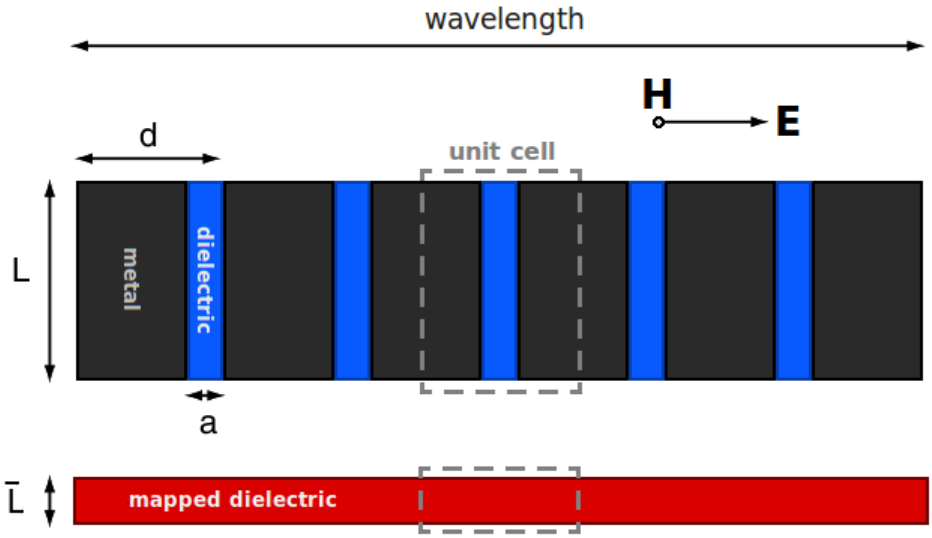

Figure 4.1: The metal-dielectric grating has thickness, L. Between the metal slits, the dielectric material has a linear permittivity, ϵ_l, and a second-order nonlinearity, $\chi^{(2)}$, or a third-order nonlinearity, $\chi^{(3)}$. The structure has a periodicity length, d, and metal slit width, a, which is also the width of dielectric layer in the grating. The grating is constructed at subwavelength scaled, meaning light is greater than the periodicity of the grating. From this, a local field enhancement between the metal slits is a result of TEM modes present in subwavelength metallic arrays at TM polarized light normally incident to the surface.

polarization will not be considered in this thesis. (3) The incidence of light is normal the grating film interface. This is assumed for simplicity in this analysis, although not necessary. In general, as long as the TM polarization is maintained, any incidence will achieve transmission and field enhancement. (4) The metal is assumed to be a perfect-electric conductor (PEC) which means the electric field is zero at all points within the metal. This assumption helps to greatly reduce the computational loads, and simplifies the analysis. Although no metal in nature is PEC, at long wavelengths of light, up to the mid-infrared, external electric fields display little penetration, making this assumption valid. (5) The material definitions of linearity and nonlinearity of the dielectric materials between the slits is assumed to have the same form as discussed in Chapter 2. (6) Both metal and dielectric materials are assumed to have no absorption, dispersion, or other losses. Again, this is made to make the analysis focused on nonlinear enhancement. However, losses due to imperfect electric conduction effects in metals will be given treatment in Chapter 5. With these assumptions

in place, the transmission and local field enhancement of metal-dielectric gratings at subwavelength scales are discussed in detail.

4.1.2 Transmission through Subwavelength Gratings

The thought of light fully transmitting through a densely layered metal-dielectric grating may seem impossible, especially considering that the grating is mostly composed of metal which does not permit light penetration. However, two points are missed in this thought. The first point is that dimensionality of the metal-dielectric grating relative to incident light is at subwavelength scales. This criterion implies that light behaves fully "wave-like" with respect to its interaction with the grating, which allows for interesting dynamics to occur. If light were not these scales, it would behave "ray-like", in which most of the light would bounce off the metal like mirror, creating only partial, diffracted transmittance. The second point is that light does not fully transmit over all grating thicknesses. Only at specific grating thicknesses at a particular frequency can a metal-dielectric grating have perfect transmission. For most grating thicknesses, only very low partial transmittance occurs.

The transmission properties of metal-dielectric grating is clearly seen the example transmission spectrum shown in Figure 4.2. Here, the sharp peaks of the transmission spectrum are the frequencies that fully transmit at the film thickness chosen. This is known as the resonance condition. However, these transmission peaks are discrete. The majority of the frequencies are at very low partial transmittance, known as off-resonance conditions. It is noted that where the transmission peak occurs is highly dependent on the grating thickness. To yield full transmission at a particular frequency, the film thickness must be tuned accordingly.

4.1.3 Local Field Enhancement

The source of enhanced optical nonlinearity in metal-dielectric gratings is in the utilization of local field enhancement caused by its transmission properties at subwavelength scales. As seen in the preceding subsection, metal-dielectric gratings allow for partial to full transmission of light at subwavelength scales. Recall, at these scales,

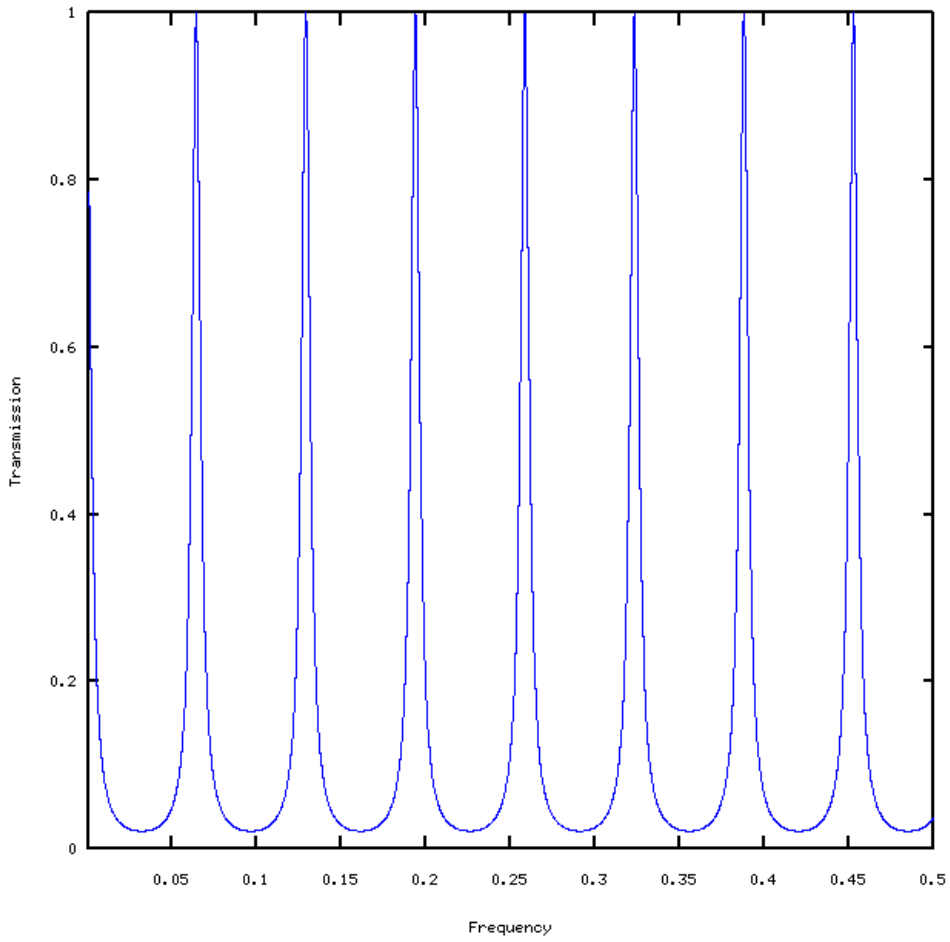

Figure 4.2: Shown is the linear transmission spectrum of a subwavelength metal-dielectric grating. Sharp peaks of the transmission spectrum are the frequencies that fully transmit at the resonance condition. Only at specific grating thicknesses at a particular frequency can a metal-dielectric grating have perfect transmission. The units of frequency are normalized with the length unit set at a micron.

light is much larger than the periodicity of the grating. Also recall that the metal is assumed to be perfect, under which no light is allowed to penetrate. Thus, for light to pass through the grating, it can only do so through the dielectric slits, which does permit light. However, under these conditions, the very large light compared to the slits must "squeeze" through, resulting in a significant increase in the field strength within the slit region as shown in Figure 4.3. The local field enhancement within the slit results from energy, flux, and electric potential conservation in the slit region.

Since the light is condensed within the slit, to maintain these quantities, the electric field strength must significantly increase, hence producing local field enhancement. By cleverly using a nonlinear material as the dielectric material in the slits, it experiences a much larger field as compared to the incident field. Averaging over the slit region, the far-field transmitted light from the nonlinear metal-dielectric grating has a larger nonlinear response. It is through this process the metal-dielectric grating generates enhanced nonlinearity.

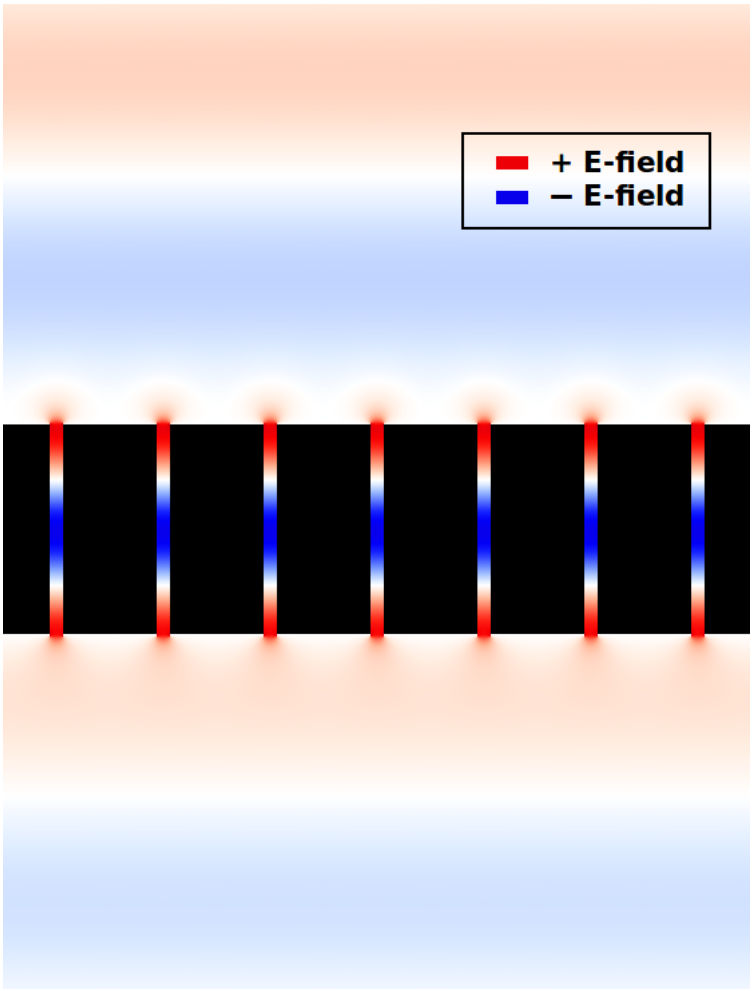

Figure 4.3: A local field enhancement between the metal slits is a result of TEM modes present in subwavelength metallic arrays at TM polarized light normally incident to the surface. Effectively, light must squeeze the dielectric layers as the metal in the grating array is assumed to be PEC. When a nonlinear material is placed as the dielectric layer, the overall nonlinearity of the material is enhanced.

4.2 Simple Scaled Mapping

From the physical understanding established in the first section, the metal-dielectric grating at subwavelength scales produces local field enhancement between the metal slits. Thus, it is expected that by placing a nonlinear material between the slits, on average, the overall nonlinear response of the grating should be larger than the nonlinearity of the nonlinear material itself. However, although the previously derived physical understanding was qualitatively correct, its quantitative features are necessary to completely understand the enhancement in nonlinearity. Thus, to provide a deeper physical understanding of the grating, a simple scaled mapping between the metal-dielectric grating and a homogeneous dielectric slab is established. Mapping to a nonlinear homogeneous dielectric slab allows the metal-dielectric grating to be better understood using a nonlinear system that is well-known. The goal of the scaled mapping is to produce the identical nonlinear optical response of the metal-dielectric grating at far-field. Through this mapping, we can better understand the physical properties, as well as predict the nonlinear optical phenomena of the grating by employing the knowledge of the nonlinear dielectric systems. In this section, a simple scaled mapping is derived between a nonlinear metal-dielectric grating and a nonlinear homogeneous dielectric slab. Also, errors associated with the mapping are calculated and explained. From the analysis, it will be shown that the metal-dielectric grating achieves multiple orders of magnitude enhancement atop of the slit constituent nonlinear material properties, and that the enhancement of optical nonlinearity is entirely controlled by the geometry of the grating structure.

4.2.1 Unit Cell Correspondence

To establish the simple scaled mapping, mathematical relationships are needed to connect the physical quantities of the metal-dielectric grating to a representative homogeneous dielectric slab. There are many different techniques to accomplish this task ranging from the whole of the Maxwell equations to transformation optics. However, the technique employed in this thesis is a unit cell correspondence, in which the energy, flux, and electric potential in the unit cell of the metal-dielectric grating is conserved in the unit cell of the homogeneous dielectric slab [37]. The unit cell of

the metal-dielectric grating is one full periodicity of the grating. The homogeneous dielectric slab however, does not have a unit cell due to its uniformity. Instead, a grating periodicity width of the dielectric slab is used as its unit cell, as this provides the best connection between the two systems in the conservation of physical quantities. A pictorial representation of this is described in Figure 4.4.

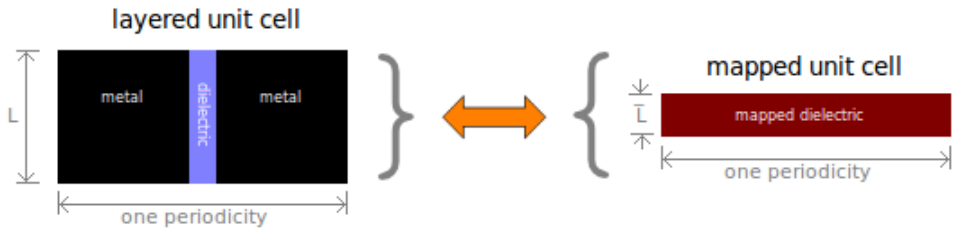

Figure 4.4: Shown is the proposed simple scaled mapping from the unit cell of the subwavelength metal-dielectric grating into a homogeneous dielectric slab. For comparison purposes, the mapped homogeneous dielectric slab is analyzed over the periodicity width of the grating.

To begin the scaled mapping, consider the electric field in the material between the metal slits, $\mathbf{E}$, and the electric field in the dielectric slab, $\bar{\mathbf{E}}$. Hereafter, optical parameters associated with the simple scaled mapping to the homogeneous dielectric slab are denoted with a bar; quantities without a bar are those of the grating system. The potential difference over one periodicity in the grating is $a \cdot \mathbf{E}$, since the metal is assumed to be PEC, and thus, the field cannot penetrate it. The potential difference over one periodicity of the dielectric slab is then $d \cdot \bar{\mathbf{E}}$. In equivalence, the electric field becomes the following.

$$\mathbf{Ea} = \bar{\mathbf{E}}\mathbf{d} \tag{4.1}$$

Solving for $\bar{\mathbf{E}}$, the electric field within mapping becomes

$$\bar{\mathbf{E}} = \frac{\mathbf{E}}{d/a} \tag{4.2}$$

This relation, derived using electric potential differences, yields the scaled mapping to the electric field. From this, the electric field is enhanced by a factor d/a. Although this is not the end, it is a promising start as $d/a > 1$, which constitutes an enhancement. Similarly, requiring the instantaneous power flow across the surface to

be equivalent, the following expression is found.

$$\left(\bar{\mathbf{E}} \times \bar{\mathbf{H}}\right) \times d = (\mathbf{E} \times \mathbf{H}) \times a \tag{4.3}$$

By applying the electric field scaled mapping into the above equation, it yields

$$\bar{\mathbf{H}} = \mathbf{H} \tag{4.4}$$

the scaled mapping for magnetic fields. Interestingly, the magnetic field between both systems remain unchanged. However, this is not surprising as the perfect metal slit squeezes the electric field, resulting in an enhancement, whereas the magnetic field is pointing parallel to the slits, and thus unaffected. To complete the scaled mapping, the film thicknesses and permittivities must be found. This requires using the last physical connection, energy. Using this, the following expression is found.

$$\frac{1}{2}\left(\bar{\epsilon}\bar{\mathbf{E}}^2 + \bar{\mu}\bar{\mathbf{H}}^2\right) \times \bar{L} \times d = \frac{1}{2}\left(\epsilon\mathbf{E}^2 + \mu\mathbf{H}^2\right) \times L \times a \tag{4.5}$$

Analyzing this expression, the scaled mapping yields a family of solutions. Using the free parameter s, any number of mappings can be found with result material properties and thicknesses as follows.

$$\bar{\mu} = \frac{a}{d}s \qquad \bar{\epsilon} = \frac{d}{a}s\epsilon \qquad \bar{L} = \frac{L}{s} \tag{4.6}$$

Choosing different s allows the mapping to become purely dielectric, purely magnetic, or a hybrid system [38]. Since most nonlinear dielectric materials of interest have $\bar{\mu} = \mu = 1$, it follows the mapping should as well. To achieve this, it fixes the free parameter as $s = d/a$, so that $\bar{\mu} = \mu = 1$, and as a result, the film thickness becomes

$$\bar{L} = \frac{L}{(d/a)} \tag{4.7}$$

and the permittivity scaling condition becomes

$$\bar{\epsilon} = \left(\frac{d}{a}\right)^2 \epsilon \tag{4.8}$$

This central result shows that the total permittivity is enhanced by $(d/a)^2$. By expressing the electric field in the mapped slab, it follows that a grating with a second-order nonlinearity has a permittivity scaling as

$$\bar{\epsilon} = \left(\frac{d}{a}\right)^2 \epsilon_l + \left(\frac{d}{a}\right)^3 \chi^{(2)} \left|\bar{\mathbf{E}}\right| \tag{4.9}$$

and a third-order nonlinearity has a permittivity scaling as

$$\bar{\epsilon} = \left(\frac{d}{a}\right)^2 \epsilon_l + \left(\frac{d}{a}\right)^4 \chi^{(3)} \left|\bar{\mathbf{E}}\right|^2 \tag{4.10}$$

Thus, the scaling condition for the linear permittivity becomes

$$\bar{\epsilon_l} = \left(\frac{d}{a}\right)^2 \epsilon_l \tag{4.11}$$

Similarly, the scaling condition for the second-order nonlinearity becomes

$$\bar{\chi^{(2)}} = \left(\frac{d}{a}\right)^3 \chi^{(2)} \tag{4.12}$$

and third-order nonlinearity becomes

$$\bar{\chi^{(3)}} = \left(\frac{d}{a}\right)^4 \chi^{(3)} \tag{4.13}$$

In general, for higher orders of nonlinearity, that the scaling condition becomes

$$\bar{\chi^{(n)}} = \left(\frac{d}{a}\right)^{n+1} \chi^{(n)} \tag{4.14}$$

From the simple scaled mapping, it is clear that the enhancement of nonlinearity is many orders of magnitude and is entirely controlled by the geometry of the grating. For example, a grating with geometry $d/a = 10$ delivers an enhancement of 1000 for second-order materials or an enhancement of 10000 for third-order materials. Equivalently, this enhancement allows for the reduction of input laser light intensity by many orders of magnitude to observe identical nonlinear optical phenomenon. For example, in the previous cases, laser light would be reduced over three to four orders

of magnitude in observation of an equivalent nonlinear response. In addition, the enhancement is frequency independent, which is crucial as nonlinear optical phenomena can only be observed at specific frequencies of light.

4.2.2 Simple Scaled Mapping Convergence

To determine the accuracy of the simple scaled mapping, a test of the transmission of a metal-dielectric grating was compared to its mapping. To simplify the test, only the linear part of the mapping was used, as nonlinear phenomena, such as producing of optical bistability and resonance in harmonic generation, are highly dependent upon linear characteristics. Thus, any small difference in the linear part who dramatically change the outcome in the nonlinear part.

In this test, the convergence of the transmission response of simple scaled mapping compared to that of the metal-dielectric grating was analyzed. Here, two variables in the grating were varied, the degree of relative subwavelength, λ/d, and enhancement factor, d/a. The variations were all compared to the resulting scaled mapping response. For simplicity, the simple scaled mapping was set to yield perfect transmission. Thus, any differences with the response of the metal-dielectric grating would yield off-resonance transmission.

The results of the convergence test are seen below in Table 4.1. Here the axes represent the two variables, d/a and λ/d with the bulk of the table showing the resulting difference between the metal-dielectric grating and corresponding simple scaled mapping. Two trends become evident in the analysis of Table 4.1. The first trend is increasing the degree of subwavelength in the grating results in a better mapped response. For example, for $\lambda/d = 40$, most of the gratings have less than one percent error with the scaled mapping. The second trend is increasing d/a in the grating results in a worse mapped response. For example, at $\lambda/d = 10$, when $d/a = 2$, its error is 0.72 percent versus when $d/a = 20$ where its error is 13.5 percent.

From these results, it is concluded that the simple scaled mapping is only accurate for deep subwavelength gratings, i.e. $\lambda/d >> 1$. At this junction, one may argue that simply designing gratings to be at very large degrees of subwavelength solves the

Linear Percent Error in Simple Scaled Mapping							
d/a	λ/d						
	2	3	4	5	10	20	40
2	19.310	8.2891	4.6089	2.9342	0.72848	0.18181	0.04543
3	44.771	23.631	14.234	9.4195	2.4669	0.62417	0.15651
4	58.943	35.710	23.029	15.813	4.3792	1.1251	0.28324
5	67.117	44.394	30.145	21.342	6.2169	1.6212	0.40972
10	82.029	64.782	50.092	38.790	13.471	3.7308	0.95854
20	88.933	76.786	64.500	53.502	22.104	6.6034	1.7355
50	93.355	85.483	76.486	67.376	33.818	11.302	3.0853

Table 4.1: Linear errors between the simple scaled mapping and metal-dielectric grating. Deeper degrees of subwavelength improves simple scaled mapping, but greater enhancement reduces mapping.

problem. This argument is definitely mathematically true, but alas physically unrealizable, as most gratings at these very large degrees of subwavelength are not possible to construct. For example, a grating is designed to achieve large enhancement, $d/a = 10$ for light at $\lambda = 10\mu m$. To better mapping, the degree of subwavelength was chosen to be $\lambda/d = 40$, so that from Table 4.1, the linear error difference is less than one percent. This design would require slit widths of 25 nm, which are difficult to construct, not to mention impractical for the rather large input wavelength. Also, such small slits would be very lossy when real metal effects were accounted. Thus, a more practical solution is needed by the means of a general scaled mapping which is fully accurate over all degrees of subwavelength and enhancement factors.

4.3 General Scaled Mapping

From the results of the previous section, a simple scaled mapping was derived using a unit cell correspondence of physical quantities between a nonlinear dielectric grating and a nonlinear dielectric slab. From the simple scaled mapping, enhancement factors for both linear and nonlinear parts of the relative permittivity were observed and generated via the ratio of grating periodicity to slit width, d/a. However, further analysis of the simple scaled mapping found it to be accurate for gratings with a very large degree of subwavelength, $\lambda/d >> 1$. For the a scaled mapping to be fully

predictive and practical, it must be accurate over all degrees of subwavelength. In this section, a general scaled mapping is derived. Through small modification of the linear permittivity to eliminate all linear errors, a general scaled mapping is reached.

4.3.1 Linear and Nonlinear Corrections

The permittivity scaling condition, $\bar{\epsilon} = \left(\frac{d}{a}\right)^2 \epsilon$, previously derived is asymptotically exact at deep subwavelength scales, $\lambda/d >> 1$. To extend this to all subwavelength scales, a general scaled mapping is derived. To accomplish this, only the linear solutions of the metal-dielectric grating and homogeneous dielectric slab in transmission need to be considered. By modifying the linear permittivity of the simple scaled mapping as

$$\bar{\epsilon_l} = \epsilon_c \left(\frac{d}{a}\right)^2 \epsilon_l \tag{4.15}$$

an identical linear transmission response of grating $T_{mapped} = T_{grating}$ can be yield. The linear dielectric correction ϵ_c can be found by setting the calculated transmission of the grating, $T_{grating}$, to the the solution of transmission through a dielectric slab, and is calculated using the following expression

$$T_{grating}^{-1} = 1 + \frac{\left((d/a)^2 \epsilon_l \epsilon_c - 1\right)^2}{4 (d/a)^2 \epsilon_l \epsilon_c} \sin^2 \left(\frac{2\pi}{\lambda} \bar{L} (d/a) \sqrt{\epsilon_l \epsilon_c}\right) \tag{4.16}$$

Here, the rather complicated expression on the right is the analytical solution for transmission of dielectric slab for light at normal incidence. The exact solution for the transmission of the metal-dielectric grating can be found as well for the same conditions, but is even more complicated, and omitted. Its solution can be found here [39]. The modification of the mapped linear permittivity slightly alters the fields within the slab, $\bar{E_c}$, and because of this, requires a modification to the nonlinear part of the permittivity as

$$\bar{\chi^{(2)}} = \chi_c^{(2)} \left(\frac{d}{a}\right)^3 \chi^{(2)} \tag{4.17}$$

and

$$\bar{\chi^{(3)}} = \chi_c^{(3)} \left(\frac{d}{a}\right)^4 \chi^{(3)} \tag{4.18}$$

The nonlinear dielectric corrections $\chi_c^{(2)}$ and $\chi_c^{(3)}$ are found by dividing the calculated fields within the slit of metallic arrays by the fields of the dielectric slab, and the corrections are expressed as as $\chi_c^{(2)} = \left(\frac{E}{(d/a)\bar{E}_c}\right)^3$ for second-order nonlinearity and $\chi_c^{(3)} = \left(\frac{E}{(d/a)\bar{E}_c}\right)^4$ for third-order nonlinearity. Calculation of all three corrections yield a more accurate mapped response of the grating and are completely determined from the linear solutions of the metal-dielectric grating and dielectric slab in transmission.

It is worth noting that all three corrections are fully predictable by means of analytical expressions, not merely "fudge factors" to make the scaled mapping work. In essence, the general scaled mapping eliminates linear error by means of aligning the linear transmission spectra over a broadband of frequencies. Also, these corrections are very small, on the order of 1 percent, and still produce the same order of magnitude enhancement to nonlinear materials. When ϵ_c is small, $\chi_c^{(2)}$ and $\chi_c^{(3)}$ are essentially one. Through this procedure, a general scaled mapping is produced with great accuracy over all subwavelength scales, and thus completes the general scaled mapping. From here, it is used and tested in the next chapter over a range of nonlinear phenomena and intensities.

Chapter 5

Demonstration of Enhancement in Metal-Dielectric Gratings

In this chapter, the nonlinear enhancement of metal-dielectric gratings is demonstrated in harmonic generation and optical bistability. Also, the scaled mapping is validated at the same field inputs as the metal-dielectric grating. In addition, special treatment is given to real-metal effects and off-resonance scaled mapping. Through these collective efforts, the enhancement properties of metal-dielectric gratings is established.

5.1 Overview of Methodology

With the background and theory in place, the nonlinear enhancement of metal-dielectric gratings can now be validated and demonstrated. Although nonlinear optics offers many useful and interesting phenomena, it would be very difficult to demonstrate the enhancement of the grating in every type. Therefore, only the most fundamental nonlinear phenomena are given treatment, that is second harmonic generation, third harmonic generation, and optical bistability.

Due to the field dependence of the nonlinearity, validation could not accomplished through direct calculation of the Maxwell equations. Instead, the validation was performed using many rigorous numerical calculations of the far-field transmission for both the metal-dielectric grating and the general scaled mapping. Specifically, the electrodynamic calculations were processed using the finite-difference time-domain

(FDTD) numerical method, and the MEEP simulation software used in all cases [40]. Information regarding the specific computational methodologies related to either nonlinear metal-dielectric gratings or nonlinear homogeneous dielectric slabs can be found in Appendix A and Appendix B. In Appendix A, an overview of the finite difference method and FDTD is discussed. In Appendix B, system specific error analysis and convergence of metal-dielectric gratings and homogeneous dielectric slabs is given.

To give a full analysis, the enhancement of metal-dielectric gratings and the robustness of the general scaled mapping is demonstrated through fundamental nonlinear optical phenomena, specifically harmonic generation in second-order and third-order nonlinear materials, and optical bistability. To contrast the enhancement of the nonlinear response from the grating, reference slabs containing the nonlinear material within the grating are also demonstrated. Thus, an enhanced response in harmonic generation from metal-dielectric gratings would yield orders of magnitude increase in frequency generation efficiency compared to the reference slabs for the same field input. Similarly, an enhanced response in optical bistability from metal-dielectric gratings would yield bistability thresholds at intensities orders of magnitude lower compared to reference slabs. For both cases, the general scaled mapping would overlap the response of the metal-dielectric gratings, confirming the prediction. In particular for bistability, the scaled mapping includes correct off-resonance transmission, and maps both upper and lower branches. From the results of each case, we will have collectively established the orders of magnitude enhancement of metal-dielectric gratings and the accuracy of the general scaled mapping for different grating thicknesses, periodicities, and intensities.

In addition to these case, two non-ideal cases are considered. The first case is the calculation of the nonlinear response of metal-dielectric gratings containing real metal. In particular, the real metal is assumed to be silver and the enhancement is demonstrated in second harmonic generation. The second case is further treatment of off-resonance mapping of the general scaled mapping. In particular, the metal-dielectric grating is assumed to have perfect electric conduction, but the film is adjusted to be off-resonance. The enhancement is demonstrated in third harmonic generation.

Although the grating as proposed produces an enhancement for any suitable wavelength maintaining the assumptions of the analysis, demonstration is focused to the mid-infrared region of light at 10.6 μm in both harmonic generation and optical bistability. The remaining sections of this chapter detail the cases described above. Physical materials and geometric structures are tabulated. Also, graphs depicting orders of magnitude enhancement are supplied.

5.2 Second-Harmonic Generation

In this section, the enhancement of metal-dielectric gratings is demonstrated and validated in second harmonic generation. The enhanced response is compared to reference slabs containing the nonlinear material between the metal slits. Also, the general scaled mapping is shown against the response of the grating.

5.2.1 Grating System

In demonstration of enhanced second harmonic generation, the metal-dielectric grating was suitably designed to efficiency produce the phenomena. To generate second harmonics, a second order nonlinear material is required. For wave mixing at 10.6 μm, Copper Chloride (I) was chosen, and was used as the dielectric layering between the metal slits. The metallic grating was designed with subwavelength periodicity. Lastly, the grating thickness was tuned for optimal conversion near resonance. The specific physical quantities for this metal-dielectric grating are found below in Table 5.1.

5.2.2 General Scaled Mapping

Using the physical quantities of the designed metal-dielectric grating for second harmonic generation, the general scaled mapping to a homogeneous dielectric slab was obtained. The mapping quantities are found in Table 5.2 below.

SHG metal-dielectric Grating Parameters	
λ	10.6 μm
d	1.325 μm
a	0.165 μm
d/a	8
λ/d	8
L	11.2 μm
ϵ_l	3.5834
$\chi^{(2)}$	13.4 pm/V

Table 5.1: Metal-dielectric grating parameters in second harmonic generation

SHG Scaled Mapping Parameters	
λ	10.6 μm
$\bar{L}$	1.4 μm
$\bar{\epsilon}_l$	229.34
$\bar{\chi}^{(2)}$	6860 pm/V
$\bar{\epsilon}_c$	1.009242
$\bar{\chi}_c^{(2)}$	1
$\bar{\epsilon}_l/\epsilon_l$	64
$\bar{\chi}^{(2)}/\chi^{(2)}$	512

Table 5.2: General scaled mapping parameters in second harmonic generation

From the general scaled mapping, the designed metal-dielectric grating is predicted to have an enhancement in linear permittivity of 64 and an enhancement in second-order nonlinearity of 512 for Copper Chloride (I). This prediction results in nearly three-orders of magnitude enhancement in second-order nonlinearity.

5.2.3 Reference Slabs

Although the predicted enhancement is many orders of magnitude larger than the base optical properties of CuCl(I), it does not necessary guarantee orders of magnitude enhancement in second harmonic generation, as it is dependent on the overall optical response of grating, not just the second-order nonlinearity. Because of this, reference slabs of Copper Chloride (I) at various thicknesses are calculated at the

same field inputs as the metal-dielectric grating containing CuCl(I) (and corresponding scaled mapping). For proper comparison, two slab thicknesses were chosen. The first slab thickness represents the best case comparison, where the slab thickness is set on resonance and contains the same number of index wavelengths within the reference slab as the grating system contains. For this case, the slab thickness is equal to the grating thickness. The second slab thickness represents the worst case comparison, where the slab thickness is set off resonance and is set at the thickness of the general scaled mapping. These two reference slab thicknesses represent an envelope of comparison for second harmonic generation to the metal-dielectric grating designed with CuCl(I).

5.2.4 Results

In Figure 5.1, the calculated response of second harmonic generation in the metal-dielectric grating containing CuCl(I) (black dots), general scaled mapping (red line), and reference slabs of CuCl(I) (blue lines) is shown. The horizontal axis represents the field input to the collective systems, where all were calculated at the same field inputs. The vertical axis represents second harmonic generated by the collective systems. For continuity purposes, the field input is normalized such that it scales the magnitude of the nonlinear part of the permittivity over the linear permittivity. For second-order nonlinear materials, the normalization is defined as $\frac{\chi^{(2)}|E_0|}{\epsilon_l}$. For this demonstration of second harmonic generation, the field inputs were kept very small, on the order of 10^{-5} normalized, to keep the growth of the second harmonic quadratic in all systems for proper comparison. Also, the second harmonic transmission was also normalized to the input field as $I_{2\omega}/I_0$.

In Figure 5.1, the enhancement of second harmonic generation in metal-dielectric gratings is observed. Compared to the best-case in the reference slab envelope, the efficiency of the metal-dielectric gratings is over 400 times greater, greater than two orders of magnitude. This implies for larger d/a, the grating with produce greater enhancement of second harmonic generation. In addition, the response of the general scaled mapping overlaps well with the response of the metal-dielectric grating. This confirms the use of the general scaled mapping as a predicting tool for systems

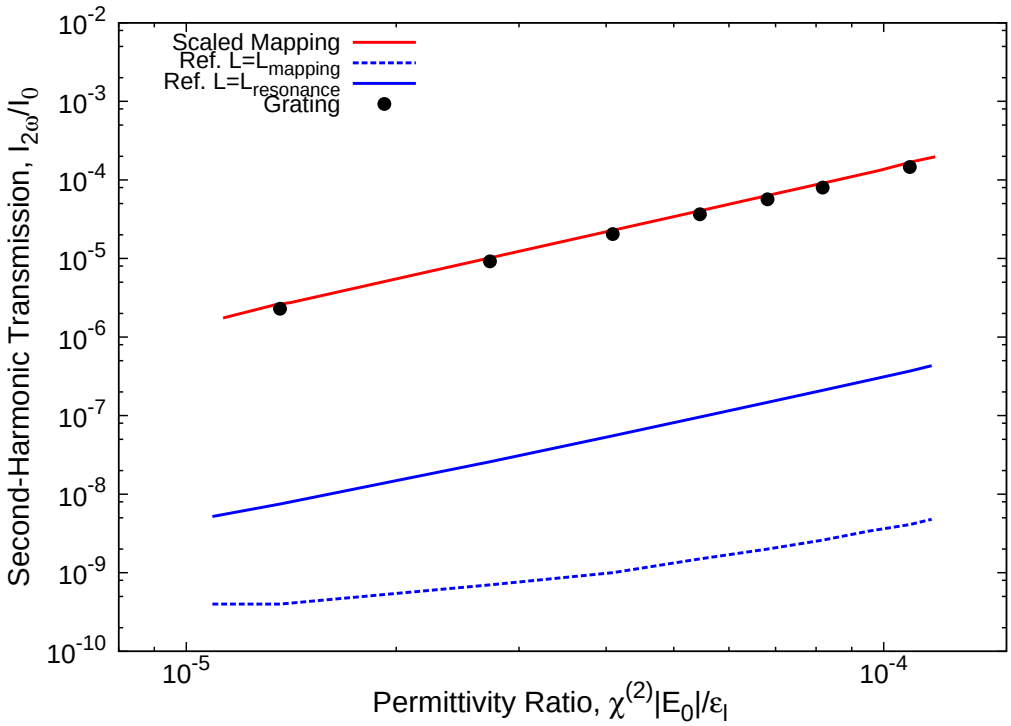

Figure 5.1: Far-field transmission, $I_{2\omega}/I_0$, of the metal-dielectric grating containing CuCl(I) in second harmonic generation. From an input light at $10.6\mu m$, the metal-dielectric grating with $d/a = 8$ at subwavelength scales, show as black dots, yields an second harmonic conversion efficiency 450 times larger compared to the references slab containing CuCl(I) used in the grating, blue lines. Also, the scaled mapping, red line, maps very well to the optical response of the grating. The input field strength is presented as a ratio defined as $\frac{\chi^{(2)}|E_0|}{\epsilon_l}$ for second-order materials, which scales the magnitude of the nonlinear part of the permittivity over the linear permittivity. The second harmonic generation shown is an small field inputs, as the nonlinear part is roughly 10^{-4} the linear part for this comparison. This plot validates the enhancement properties of the metal-dielectric grating and scale mapping in second harmonic generation.

in second harmonic generation. From these conclusions, the orders of magnitude enhancement of second harmonic generation in metal-dielectric gratings is confirmed.

5.3 Third-Harmonic Generation

In this section, the enhancement of metal-dielectric gratings is demonstrated and validated in third harmonic generation. The enhanced response is compared to reference slabs containing the nonlinear material between the metal slits. Also, the general scaled mapping is shown against the response of the grating.

5.3.1 Grating System

In demonstration of enhanced third harmonic generation, the metal-dielectric grating was suitably designed to efficiency produce the phenomena. To generate third harmonics, a third order nonlinear material is required. For wave mixing at 10.6 μm, Gallium Arsenide was chosen, and was used as the dielectric layering between the metal slits. The metallic grating was designed with subwavelength periodicity. Lastly, the grating thickness was tuned for optimal conversion near resonance. The specific physical quantities for this metal-dielectric grating are found below in Table 5.3.

THG metal-dielectric Grating Parameters	
λ	10.6 μm
d	0.800 μm
a	0.100 μm
d/a	8
λ/d	13.25
L	3.352 μm
ϵ_l	10.13
$\chi^{(3)}$	$1.49 * 10^{-19} pm^2/V^2$

Table 5.3: Metal-dielectric grating parameters in third harmonic generation

5.3.2 General Scaled Mapping

Using the physical quantities of the designed metal-dielectric grating for third harmonic generation, the general scaled mapping to a homogeneous dielectric slab was obtained. The mapping quantities are found in Table 5.4 below.

THG Scaled Mapping Parameters	
λ	10.6 μm
$\bar{L}$	0.419 μm
$\bar{\epsilon}_l$	644
$\bar{\chi}^{(3)}$	$7390 * 10^{-19} pm^2/V^2$
$\bar{\epsilon}_c$	1.0066425
$\bar{\chi}_c^{(3)}$	1
$\bar{\epsilon}_l/\epsilon_l$	64
$\bar{\chi}^{(3)}/\chi^{(3)}$	4096

Table 5.4: General scaled mapping parameters in third harmonic generation

From the general scaled mapping, the designed metal-dielectric grating is predicted to have an enhancement in linear permittivity of 64 and an enhancement in third-order nonlinearity of 4096 for Gallium Arsenide. This prediction results in nearly four-orders of magnitude enhancement in third-order nonlinearity.

5.3.3 Reference Slabs

Although the predicted enhancement is many orders of magnitude larger than the base optical properties of GaAs, it does not necessary guarantee orders of magnitude enhancement in third harmonic generation, as it is dependent on the overall optical response of grating, not just the third-order nonlinearity. Because of this, reference slabs of Gallium Arsenide at various thicknesses are calculated at the same field inputs as the metal-dielectric grating containing GaAs (and corresponding scaled mapping). For proper comparison, two slab thicknesses were chosen. The first slab thickness represents the best case comparison, where the slab thickness is set on resonance and contains the same number of index wavelengths within the reference slab as the grating system contains. For this case, the slab thickness is equal to the grating thickness. The second slab thickness represents the worst case comparison, where the slab thickness is set off resonance and is set at the thickness of the general scaled mapping. These two reference slab thicknesses represent an envelope of comparison for third harmonic generation to the metal-dielectric grating designed with GaAs.

5.3.4 Results

In Figure 5.2, the calculated response of third harmonic generation in the metal-dielectric grating containing GaAs (black dots), general scaled mapping (red line), and reference slabs of GaAs (blue lines) is shown. The horizontal axis represents the field input to the collective systems, where all were calculated at the same field inputs. The vertical axis represents third harmonic generated by the collective systems. For continuity purposes, the field input is normalized such that it scales the magnitude of the nonlinear part of the permittivity over the linear permittivity. For third-order nonlinear materials, the normalization is defined as $\frac{\chi^{(3)}|E_0|^2}{\epsilon_l}$. For this demonstration of third harmonic generation, the field inputs were kept very small, on the order of 10^{-4} normalized, to keep the growth of the third harmonic small in all systems for proper comparison. Also, the third harmonic transmission was also normalized to the input field as $I_{3\omega}/I_0$.

In Figure 5.2, the enhancement of third harmonic generation in metal-dielectric gratings is observed. Compared to the best-case in the reference slab envelope, the efficiency of the metal-dielectric gratings is over 1500 times greater, greater than three orders of magnitude. This implies for larger d/a, the grating with produce greater enhancement of third harmonic generation. The response of the metal-dielectric grating at larger field input loses linearity and plateaus. This is caused by the nonlinear part becoming large enough to push the grating system off-resonance, reducing the overall third harmonic generation. However, dividing the third harmonic field by the transmitted input frequency results in large efficiency, thus producing significant enhancement compared to the reference envelope. In addition, the response of the general scaled mapping overlaps well with the response of the metal-dielectric grating. This confirms the use of the general scaled mapping as a predicting tool for systems in third harmonic generation. From these conclusions, the orders of magnitude enhancement of third harmonic generation in metal-dielectric gratings is confirmed.

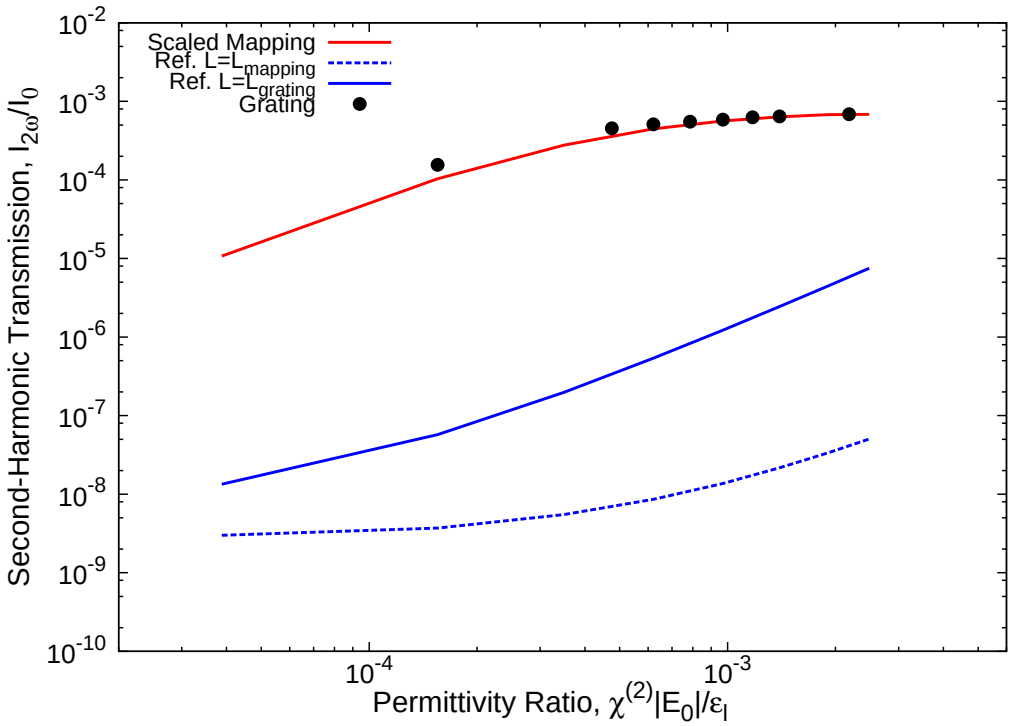

Figure 5.2: Far-field transmission, $I_{3\omega}/I_0$, of the metal-dielectric grating containing GaAs in third harmonic generation. From an input light at $10.6\mu m$, the metal-dielectric grating with $d/a = 8$ at subwavelength scales, show as black dots, yields an third harmonic conversion efficiency 1500 times larger compared to the references slab containing CuCl(I) used in the grating, blue lines. Also, the scaled mapping, red line, maps very well to the optical response of the grating. The input field strength is presented as a ratio defined as $\frac{\chi^{(3)}|E_0|^2}{\epsilon_l}$ for third-order materials, which scales the magnitude of the nonlinear part of the permittivity over the linear permittivity. The third harmonic generation shown is an small field inputs, as the nonlinear part is roughly 10^{-4} the linear part for this comparison. This plot validates the enhancement properties of the metal-dielectric grating and scaled mapping in third harmonic generation.

5.4 Optical Bistability

In this section, the enhancement of metal-dielectric gratings is demonstrated and validated in optical bistability. The enhanced response is compared to reference slabs containing the nonlinear material between the metal slits. Also, the general scaled mapping is shown against the response of the grating.

5.4.1 Grating System

In demonstration of enhanced optical bistability, the metal-dielectric grating was suitably designed to efficiency produce the phenomena. To generate bistability, a third order nonlinear material is required. For bistability at 10.6 μm, Silicon was chosen, and was used as the dielectric layering between the metal slits. The metallic grating was designed with subwavelength periodicity. The grating thickness was tuned such that it generated the first onset of bistability. The specific physical quantities for this metal-dielectric grating are found below in Table 5.5.

OBS metal-dielectric Grating Parameters	
λ	10.6 μm
d	0.883 μm
a	0.221 μm
d/a	4
λ/d	12
L	4.24 μm
ϵ_l	12.09
$\chi^{(3)}$	$7.4 * 10^{-20} pm^2/V^2$

Table 5.5: Metal-dielectric grating parameters in optical bistability

5.4.2 General Scaled Mapping

Using the physical quantities of the designed metal-dielectric grating for optical bistability, the general scaled mapping to a homogeneous dielectric slab was obtained. The mapping quantities are found in Table 5.6 below.

From the general scaled mapping, the designed metal-dielectric grating is predicted to have an enhancement in linear permittivity of 16 and an enhancement in third-order nonlinearity of 256 for Silicon. This prediction results in nearly three-orders of magnitude enhancement in third-order nonlinearity.

OBS Scaled Mapping Parameters	
λ	10.6 μm
$\bar{L}$	1.06 μm
$\bar{\epsilon}_l$	195
$\bar{\chi}^{(3)}$	$1894 * 10^{-20} pm^2/V^2$
$\bar{\epsilon}_c$	1.006445
$\bar{\chi}_c^{(3)}$	1
$\bar{\epsilon}_l/\epsilon_l$	16
$\bar{\chi}^{(3)}/\chi^{(3)}$	256

Table 5.6: General scaled mapping parameters in optical bistability

5.4.3 Reference Slabs

Although the predicted enhancement is many orders of magnitude larger than the base optical properties of Si, it does not necessary guarantee orders of magnitude enhancement in optical bistability, as it is dependent on the overall optical response of grating, not just the third-order nonlinearity. Because of this, one reference slab of Si at the first onset of optical bistability was calculated at the same field inputs as the metal-dielectric grating containing Si (and corresponding scaled mapping). The choice represents the best case comparison.

5.4.4 Results

In Figure 5.3, the calculated response of optical bistability in the metal-dielectric grating containing Si (black dots), general scaled mapping (red line), and the reference slab of Si (blue line) is shown. The horizontal axis represents the field input to the collective systems, where all were calculated at the same field inputs. The vertical axis represents transmission generated by the collective systems. For continuity purposes, the field input is normalized such that it scales the magnitude of the nonlinear part of the permittivity over the linear permittivity. For third-order nonlinear materials, the normalization is defined as $\frac{\chi^{(3)}|E_0|^2}{\epsilon_l}$. For this demonstration of optical bistability, the field inputs were not kept very small, and range from 0.01 to 10, in order to show the complete threshold of bistability for all systems. Also, the transmission was also normalized to the input field as I_ω/I_0.

In Figure 5.3, the enhancement of optical bistability in metal-dielectric gratings is observed. Compared to the reference slab, the threshold of bistability of the metal-dielectric gratings is reduced by 50 times, roughly two orders of magnitude. Lowering the threshold of optical bistability is of great importance, particularly in low-power optical computation. This implies for larger d/a, the grating with produce greater enhancement of optical bistability, by further lowering of the bistability threshold.

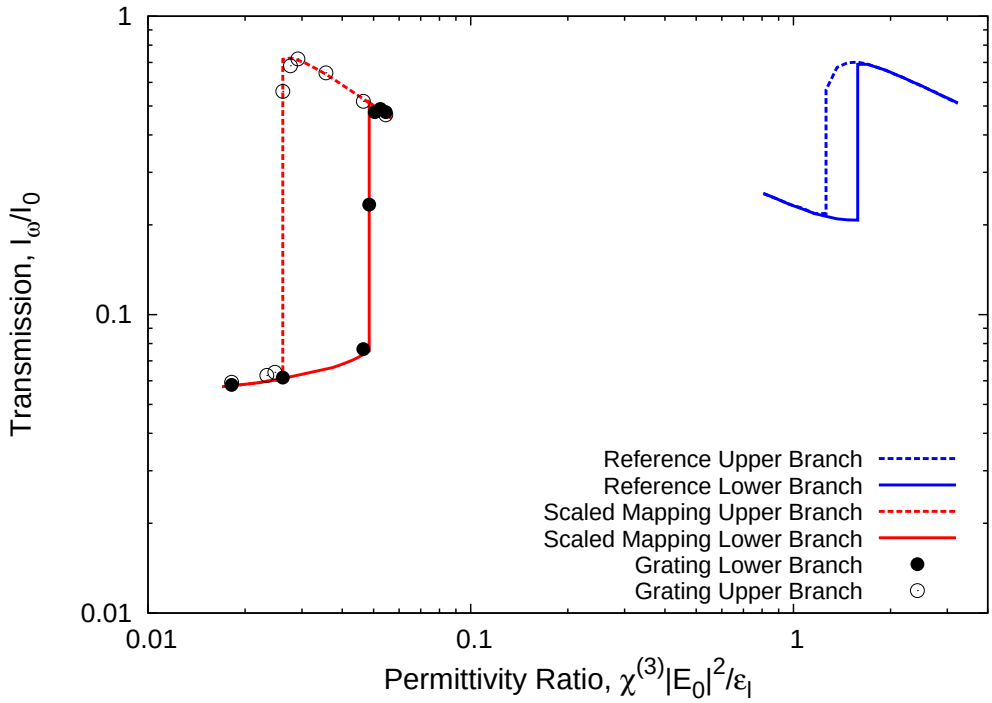

Figure 5.3: Far-field transmission, I_ω/I_0, of the metal-dielectric grating containing silicon in bistability. The bistability region of the grating occurs at over two orders of magnitude lower intensity than the references slab. Both the grating and the reference slab film thicknesses were set near the first on-set of bistability.

In Figure 5.4, the response of the general scaled mapping overlaps well with the response of the metal-dielectric grating. This of particular importance as it confirms the scaled mapping in both on resonance and off resonance situations. Also, the scaled mapping is capable of mapping to optical two state systems, predicting the threshold location and upper and lower contrast branches. From this, it confirms the use of the general scaled mapping as a predicting tool for systems in optical bistability. From these conclusions, the orders of magnitude enhancement of optical bistability in metal-dielectric gratings is confirmed.

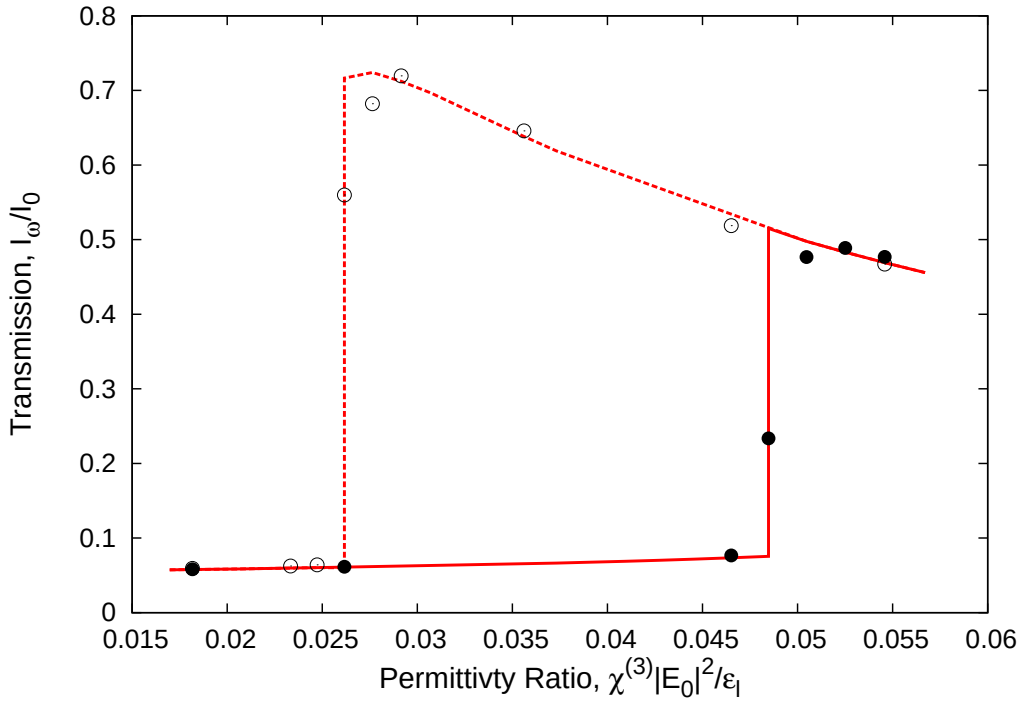

Figure 5.4: Far-field transmission, I_ω/I_0, of the metal-dielectric grating containing silicon in bistability. The general scaled mapping maps very well to the transmission of the upper and lower bistability curves, and predicts the intensity on-sets of the bistability region.

5.5 Enhancement with Real Metal

In this section, the enhancement of metal-dielectric gratings is demonstrated and validated in second harmonic generation when the PEC assumption is removed and replace with the real metal response of Silver. The enhanced response is compared to reference slabs containing the nonlinear material between the metal slits. Because the general scaled mapping is based on the PEC assumption, no mapping is shown against the response of the grating.

5.5.1 Grating System

Hardened critics of the scaled mapping analysis and previous enhanced nonlinear phenomena demonstrations would be wise to be skeptical of the enhancement of

optical nonlinearity with the assumption that metal is a perfect electric conduction, as no real metal is PEC. In general, metals are lossy, and carry some penetration depth. With these features existing, might it reduce or eliminate any enhancement of optical nonlinearity?

In demonstration of enhanced second harmonic generation with a real metal response, the metal-dielectric grating was suitably designed to efficiency produce the phenomena. To generate second harmonics, a second order nonlinear material is required. Using the same second-order nonlinear material in the previous wave mixing example, at 10.6 μm, Copper Chloride (I) was chosen, and was used as the dielectric layering between the metal slits. The metal was chosen to be metallic response of Silver at $10.6\mu m$. The metallic grating was designed with subwavelength periodicity. Lastly, the grating thickness was tuned for optimal conversion near resonance. The specific physical quantities for this metal-dielectric grating are found below in Table 5.7.

SHG metal-dielectric Grating Parameters	
λ	10.6 μm
d	3.53 μm
a	0.833 μm
d/a	4
λ/d	3
L	2.606 μm
ϵ_l	3.5834
$\chi^{(2)}$	13.4 pm/V

Table 5.7: Metal-dielectric grating parameters in second harmonic generation with Silver as grating material instead of PEC

5.5.2 General Scaled Mapping

Since the PEC condition was removed from the metal-dielectric grating, the simple and general scaled mapping derived cannot be applied to a system containing a real metal response. Also, a general scaled mapping is difficult to obtain using the methods employed in previous analysis. Thus, a general scaled mapping was not given for this case. It was seen in the previous section that when metal is PEC that the

general scaled mapping predicts the response of the metal-dielectric grating in second harmonic generation. Thus, using the general scaled mapping as a guideline, the designed metal-dielectric grating is predicted to have an enhancement in linear permittivity of 16 and an enhancement in second-order nonlinearity of 64 for Copper Chloride (I). Under the PEC assumption, this prediction results in nearly two-orders of magnitude enhancement in second-order nonlinearity. However, factoring in lossy in the metal, it should be expected to have an second-order enhancement of greater than one order of magnitude.

5.5.3 Reference Slabs

Although the predicted enhancement is many orders of magnitude larger than the base optical properties of CuCl(I), it does not necessary guarantee orders of magnitude enhancement in second harmonic generation, as it is dependent on the overall optical response of grating, not just the second-order nonlinearity. Also, with the inclusion of the real metal response in the grating, it is essential to compare to references slabs, as the general scaled mapping is unable to predict the resulting enhancement loss. Because of this, reference slabs of Copper Chloride (I) at various thicknesses are calculated at the same field inputs as the metal-dielectric grating containing CuCl(I) (and corresponding scaled mapping). For proper comparison, two slab thicknesses were chosen. The first slab thickness represents the best case comparison, where the slab thickness is set on resonance and contains the same number of index wavelengths within the reference slab as the grating system contains. For this case, the slab thickness is equal to the grating thickness. The second slab thickness represents the worst case comparison, where the slab thickness is set off resonance and is set at the thickness of the general scaled mapping. These two reference slab thicknesses represent an envelope of comparison for second harmonic generation to the metal-dielectric grating designed with CuCl(I).

5.5.4 Results

In Figure 5.5, the calculated response of second harmonic generation in the metal-dielectric grating containing CuCl(I) and Silver (black dots), and reference slabs of

CuCl(I) (blue lines) is shown. The horizontal axis represents the field input to the collective systems, where all were calculated at the same field inputs. The vertical axis represents second harmonic generated by the collective systems. For continuity purposes, the field input is normalized such that it scales the magnitude of the nonlinear part of the permittivity over the linear permittivity. For second-order nonlinear materials, the normalization is defined as $\frac{\chi^{(2)}|E_0|}{\epsilon_l}$. For this demonstration of second harmonic generation, the field inputs were kept very small, on the order of 10^{-4} normalized, to keep the growth of the second harmonic quadratic in all systems for proper comparison. Also, the second harmonic transmission was also normalized to the input field as $I_{2\omega}/I_0$.

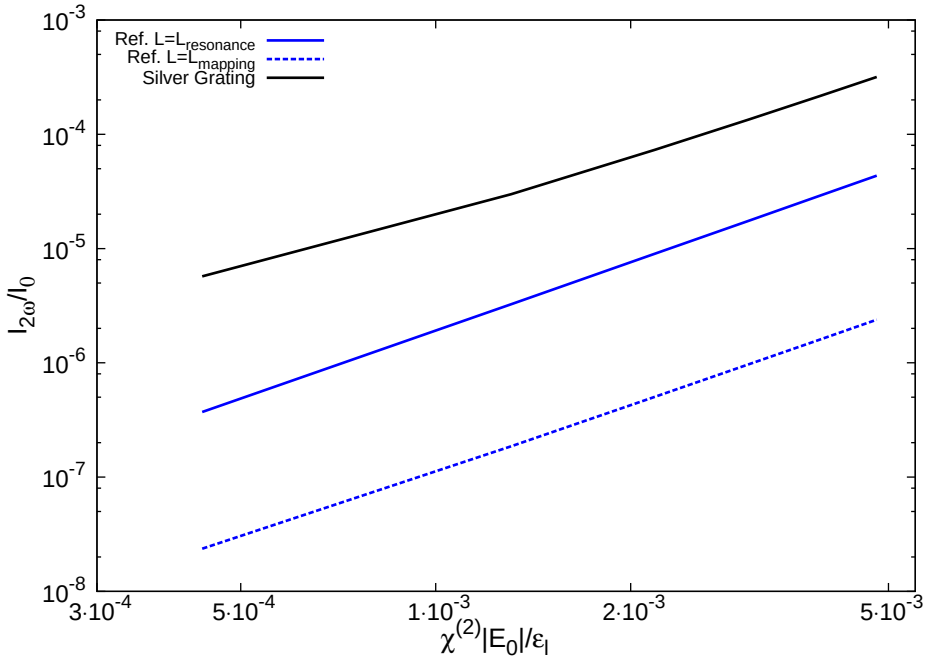

Figure 5.5: Orders of magnitude enhancement of optical nonlinearity is still achieved in grating containing lossy metal. For silver at 10.6 μm, a multi-order of magnitude enhancement is observed in CuCl as compared to multiple reference slab film thicknesses. A scaled mapping is not shown as losses from metal were not incorporated into its assumptions.

In Figure 5.5, the enhancement of second harmonic generation in metal-dielectric gratings containing the real metal response of Silver is observed. Compared to the best-case in the reference slab envelope, the efficiency of the metal-dielectric gratings is over one order of magnitude times greater as suggested from the scaled mapping

analysis. This implies for larger d/a, the grating with produce greater enhancement of second harmonic generation, although not without additional losses due to the real metal response. Also, for nonlinear materials at longer wavelengths, losses from metal will diminish, where as shorter wavelengths will reduced the effectiveness of metal due to larger field penetration into the metal. Overall, this result strengths our proposed method for enhancement of nonlinear materials, and justifies the use of lossy metal in enhancement. From these conclusions, the orders of magnitude enhancement of second harmonic generation in metal-dielectric gratings is confirmed for real metal responses of Silver.

5.6 Scaled Mapping Off-Resonance

In this section, the response of an enhanced metal-dielectric gratings is demonstrated and validated in third harmonic generation when designed to be off-resonance. In particular, this case is designed to show the accuracy and predictive power of the general scaled mapping in an off-resonance case of harmonic generation.

5.6.1 Grating System

Hardened critics of the scaled mapping analysis and previous enhanced nonlinear phenomena demonstrations would be wise to be skeptical of the capability of the general scaled mapping in an off-resonance scenario. In general, the previous analysis gave preference to the metal-dielectric grating on-resonance, and in the previous harmonic generation cases, the general scaled mapping preformed well. With these features existing, might the accuracy or prediction power of the general scaled mapping be reduce or eliminated when off-resonance?

In demonstration of this question, a metal-dielectric grating was design to have enhanced third harmonic generation, but the metal-dielectric grating was not suitably designed to efficiency produce the phenomena, i.e., the grating was design off-resonance. To generate third harmonics, a third order nonlinear material is required. Using the same third-order nonlinear material in the previous wave mixing example,

at 10.6 μm, Gallium Arsenide was chosen, and was used as the dielectric layering between the metal slits. The metallic grating was designed with subwavelength periodicity. Lastly, the grating thickness was tuned to be at the trough for off-resonance. The specific physical quantities for this metal-dielectric grating are found below in Table 5.8.

THG metal-dielectric Grating Parameters	
λ	10.6 μm
d	0.663 μm
a	0.166 μm
d/a	4
λ/d	16
L	3.6871 μm
ϵ_l	10
$\chi^{(3)}$	$1.49 * 10^{-19} pm^2/V^2$

Table 5.8: Metal-dielectric grating parameters in third harmonic generation at off-resonance

5.6.2 General Scaled Mapping

Using the physical quantities of the designed metal-dielectric grating for third harmonic generation, the general scaled mapping to a homogeneous dielectric slab was obtained. The mapping quantities are found in Table 5.9 below.

THG Scaled Mapping Parameters	
λ	10.6 μm
$\bar{L}$	0.922 μm
$\bar{\epsilon}_l$	160
$\bar{\chi}^{(3)}$	$381 * 10^{-19} pm^2/V^2$
$\bar{\epsilon}_c$	1.006746
$\bar{\chi}_c^{(3)}$	1
$\bar{\epsilon}_l/\epsilon_l$	16
$\bar{\chi}^{(3)}/\chi^{(3)}$	256

Table 5.9: General scaled mapping parameters in third harmonic generation at off-resonance

From the general scaled mapping, the designed metal-dielectric grating is predicted to have an enhancement in linear permittivity of 16 and an enhancement in third-order nonlinearity of 256 for Gallium Arsenide. This prediction results in nearly three-orders of magnitude enhancement in third-order nonlinearity.

5.6.3 Reference Slabs

For this validation case, reference slabs are not of concern. Here, the accuracy of the general scaled mapping is being tested in an off-resonance case. Thus, no reference slab are presented.

5.6.4 Results

In Figure 5.6, the calculated response of third harmonic generation in the metal-dielectric grating containing GaAs (black dots), and general scaled mapping (red line) is shown. The horizontal axis represents the field input to the collective systems, where all were calculated at the same field inputs. The vertical axis represents third harmonic generated by the collective systems. For continuity purposes, the field input is normalized such that it scales the magnitude of the nonlinear part of the permittivity over the linear permittivity. For third-order nonlinear materials, the normalization is defined as $\frac{\chi^{(3)}|E_0|^2}{\epsilon_l}$. Also, the third harmonic transmission was also normalized to the input field as $I_{3\omega}/I_0$.

In Figure 5.6, the response of the general scaled mapping overlaps well with the response of the metal-dielectric grating. Even at off-resonance, the general scaled mapping predicts the response of the metal-dielectric grating in third harmonic generation. This is not entirely unexpected as the general scaled mapping for optical bistability was validated, and this system had many points off-resonance (as necessary for optical bistability) that accurately mapped. This confirms the use of the general scaled mapping as a predicting tool for systems in third harmonic generation and for any system on or off resonance, and is thus confirmed.

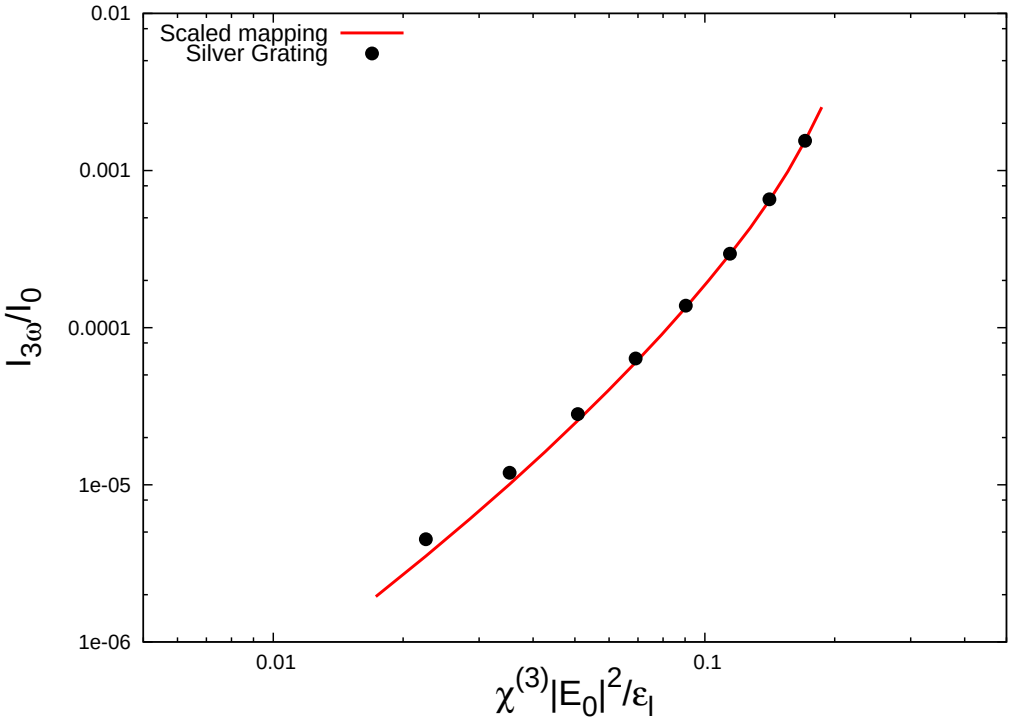

Figure 5.6: The general scaled mapping of metal-dielectric grating in third harmonic generation at off-resonance conditions accurately predicts the phenomena.

Appendix A

Numerical Simulation of Electrodynamic Systems

Many situations in science and engineering, mathematical and physical model do not easily lend themselves to analytical or exact calculation. The remedy for these situations is to use numerical methods. In this appendix, a brief introduction to numerical methods related to this thesis is provided. Here, a brief overview of the finite-difference numerical method is given. Methods for numerical simulation of electrodynamic systems known as FDTD, critical in the analysis of nonlinear metal-dielectric gratings, are discussed. Also, problem specific cases are presented in demonstration of numerical modeling.

A.1 The Finite-Difference Time-Domain Method

In the calculation of physical models in engineering and science, the majority are accomplished through numerical methods. There are a variety of numerical approximations, such as finite difference [41] and finite element methods [42], for approximation of physical and mathematical models. In the analysis of nonlinear metal-dielectric gratings throughout this thesis, the finite difference numerical method was used for calculating electromagnetic waves propagating through optical media. In this section, an introduction is given for the finite difference approximation and its application to electrodynamic theory.

A.1.1 Finite Difference Approximation

Complex systems of differential equations are difficult to solve through analytical methods. To yield solutions, physical models can be approximated and discretized using the finite difference method. To start, the domain of the physical system is discretized and made finite. To approximate the physical model along the domain, discrete points are chosen for calculation. Most finite difference methods apply a uniform discretization along each domain, although the discretization size may differ among domains.

The simplest domain to discretized is a one-dimensional line as seen in Figure A.1. Physical systems having 1-D domain are common in science and engineering and include bending of beams, electromagnetic waves in homogeneous materials, and thermodynamic heat transfer in planar structures. Here, the domain variable, x, is spatial dimension in the x-direction, and discrete points are chosen every Δx along the x-direction. Since the domain has a finite length, L, the discretization produces a total of $L/\Delta x$ points of calculation.

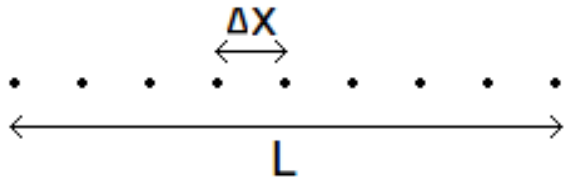

Figure A.1: Shown is a one-dimension line is discretized uniformly. Here, the line is discretized by Δx for a domain length L. Producing this discretization creates points of calculation in the approximation of physical models using the finite difference method. For this example, the discretization produces a total of $L/\Delta x$ points of calculation.

As in most numerical methods for differential equations, the finite difference method approximates the derivative operator. The finite difference approximation arises from the definition of a derivative. For a single variable function, $f(x)$, the derivative of the function, as defined below, is the difference of the function at δx by δx when it approaches zero.

$$f^{'}(x) = \lim_{\delta x \to 0} \frac{f(x + \delta x) - f(x)}{\delta x} \tag{A.1}$$

For a discretized domain, the function, $f(x)$, is approximated as

$$f^{'}(x) \approx \frac{f(x+\Delta x) - f(x)}{\Delta x} \tag{A.2}$$

where Δx is the discretization length of the domain. Here, the derivative of the function $f^{'}(x)$ at x approximated by the difference between the function $f(x)$ at x and its nearest neighbor $f(x+\Delta x)$ divided by the discretization distance Δx.

Although this approximation will work, more commonly, the approximation is created by making the difference symmetrical as seen below.

$$f^{'}(x) = \frac{f(x+\Delta x) - f(x-\Delta x)}{2\Delta x} \tag{A.3}$$

Here, the difference is taken by the two nearest neighbors, producing a total average of surrounding neighboring points. This finite difference approximation is known as the central difference.

In demonstration of the finite difference method, the function $f(x) = e^(x)$ is approximated over the domain $[0, 1]$. Now, simple calculus shows that $f^{'}(x) = e^{x}$, but for demonstration purposes, the derivative of $f(x) = e^{x}$ is approximated using the finite difference method. Using the central difference definition, the approximation is

$$f^{'}(x) = e^{x}\frac{sinh(\Delta x)}{\Delta x} \tag{A.4}$$

which is very close to the exact derivative. In fact, the term $\frac{sinh(\Delta x)}{\Delta x}$ goes to unity as Δx goes to zero. For example, choosing $\Delta x = 0.1$, $\frac{sinh(\Delta x)}{\Delta x} = 1.00167$. Making $\Delta x = 0.01$ an order of magnitude smaller yields $\frac{sinh(\Delta x)}{\Delta x} = 1.000017$. In Figure A.2, the approximations are shown for the discretization developed above. From the above considerations, the finite difference method produces accurate results for well behaved models under most computational scenarios.

The finite difference method can be easily extended to higher-order derivatives and in multi-dimensional domains. For higher-order derivatives, the one-dimensional central difference approximation is applied repeatedly to each derivative taken, as with exact calculations. As an example, the second-order central difference approximation is

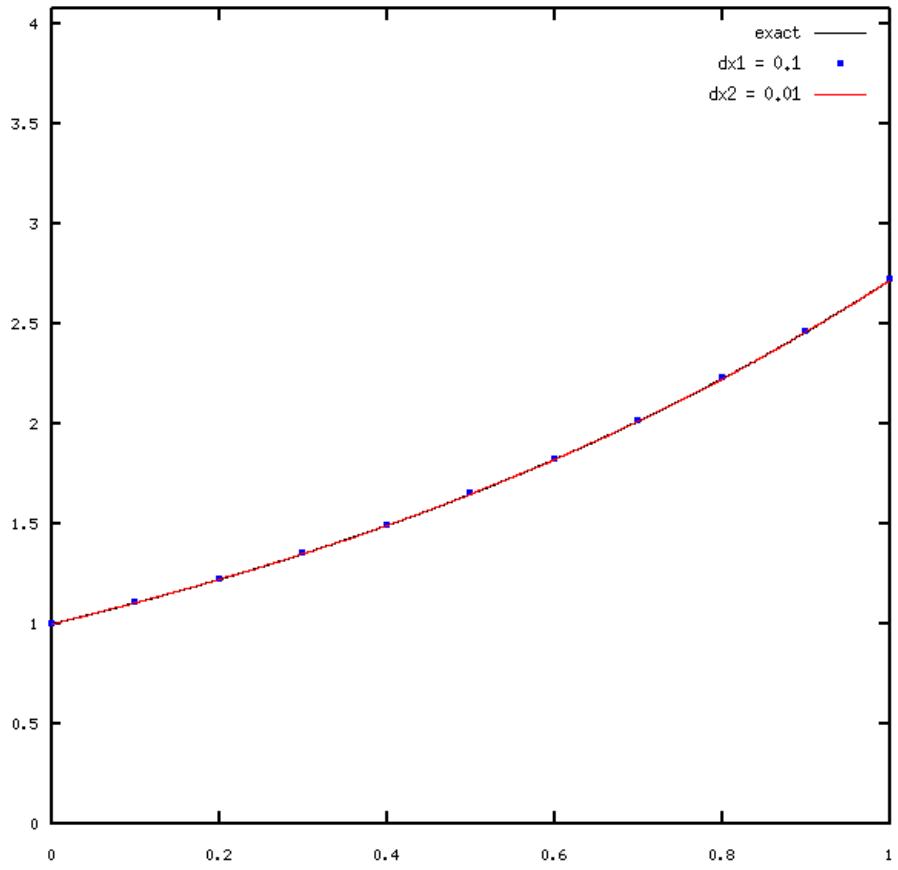

Figure A.2: Graphic representation of the finite difference approximation to $f(x) = e^(x)$ which resulted in $f^{'}(x) = e^{x}\frac{sinh(\Delta x)}{\Delta x}$. Over the domain $[0, 1]$ (horizontal-axis), the approximation of the function is plotted for the two different discretizations (vertical-axis). The large, blue, and small, red, discretization work very well, and are accurate to the second and fourth decimal place respectively.

demonstrated for a one-dimensional function.

$$f^{''}(x) = \frac{f^{'}(x + \Delta x) - f^{'}(x - \Delta x)}{2\Delta x} \tag{A.5}$$

Although this representation of the second-order derivative will work, expanding the first derivatives with its central difference approximation yields a more convenient form.

$$f^{''}(x) = \frac{f(x + 2\Delta x) - 2f(x) + f(x - 2\Delta x)}{4(\Delta x)^2} \tag{A.6}$$

In addition to higher-order derivatives, partial derivatives of multi-dimensional functions can be calculated by the finite difference method. For multi-dimensional problems, each axis of the domain must be discretized. Then, approximating partial derivatives is the same as computing exact partial derivative expressions. By holding all discretized dimensions as constants except the dimension of interest, the partial derivative approximation is determined. As an example, the one-dimensional x spatial function $f(x)$ is turned into a two-dimensional function $f(x,t)$ in space and time, t. Thus, the first partial derivative approximation with respect to x is exactly the same as the one-dimension example but now holding t as a constant within the function.

$$f_x(x,t) = \frac{f(x+\Delta x,t) - f(x-\Delta x,t)}{2\Delta x} \tag{A.7}$$

Similarly, letting Δt be the time discretization, the first partial derivative with respect to t is seen below.

$$f_t(x,t) = \frac{f(x,t+\Delta t) - f(x,t-\Delta t)}{2\Delta t} \tag{A.8}$$

This concludes the brief introduction of finite difference approximation. Finite difference method is an easy, yet robust approximation scheme to be used in the calculation of complex physical models. It is noted that further information is needed to fully implement these approximations to differential equations, partial differential equations, and systems of differential equations. In particular, convergence and stability criterion were not discussed, since it was not relevant for this introduction. From here, the following references are particularly useful for further development of finite difference methodology and practice [41].

A.1.2 Finite Differences in EM Theory

As developed in Chapter 2, the propagation of light through media in classical regimes is describe by the Maxwell equations. With simplified models, many exact expressions in optics are found using the Maxwell Equations, such as light transmitting through

linear homogeneous dielectric slabs, dispersion of materials, diffraction, and waveguided modes. However, for more complex systems, such as nonlinear materials, or empirical models, such as real metals, exact solutions are limited or impossible to be found. Therefore, the need for numerical electrodynamic approximation is necessary to explore and describe these systems. Here, a brief introduction of electrodynamic systems as approximated by the finite difference method is presented.

To model light propagation through source-free media, two of the four Maxwell Equations are necessary: Ampere's and Faraday's Law respectively (seen below), as they form the basis of wave propagation in electromagnetic theory. Note: Refer to the nomenclature of previous chapters for variable definition clarity when necessary.

$$\epsilon \frac{\partial \mathbf{E}}{\partial t} = \nabla \times \mathbf{H} \tag{A.9}$$

$$-\mu \frac{\partial \mathbf{H}}{\partial t} = \nabla \times \mathbf{E} \tag{A.10}$$

Numerical modeling of electrodynamic systems becomes necessary when media ϵ and μ have complex definitions. For example, in third-order nonlinear materials, $\epsilon = \epsilon_l + \chi^(3)|\mathbf{E}|^{\mathbf{2}}$ and $\mu = 1$. Although material μ causes no analytical problems in this example, the material ϵ does. Specifically, when solving for the electric field $\mathbf{E}$ in Ampere's and Faraday's equations, $\mathbf{E}$ must also be solved for through the material definition. In this case, a general solution is not possible, and requires numerical calculation for full treatment. To do this, Ampere's and Faraday's Laws must be approximated.

The simplest approximation to Maxwell's Equations is through the finite difference method. Using the introduction provided in the above section, finite difference method is applied to these equations. Also, it is noted that the finite difference method applied to electrodynamic systems is referred as the finite-difference time-domain method or FDTD, as coined by Allan Taflov [43]. First, the domain must be specified. The general domain for the Maxwell Equations is four-dimensional: three spatial dimensions and one time dimension. However, many electrodynamic systems do not require the full domain to be used. The simplest systems require only one

spatial dimension and the time-dimension. In general, the time-dimension always is required; time-independent electromagnetic problems can still be numerically solved using finite differences, but these are solutions of the potential equation and are not relevant to this thesis.

Next, the partial derivatives in the Ampere's and Faraday's laws are replaced with the finite difference approximation. This is the point where the FDTD approximation becomes challenging. In the previous examples, only a single function with multi-dimensional domains were considered. In the electrodynamic systems, the electric field $\mathbf{E}$ and the magnetic field $\mathbf{H}$ must both be solved, and thus, these two functions must be approximated. In addition, the electric and magnetic fields are coupled between Ampere's and Faraday's laws through curl operators, which are not as simple to numerically approximate as ordinary partial derivatives. In fact, typical finite difference implementations do not work with the Maxwell equations. This is because these yield solutions that are affected by numerical dispersion, an adverse approximation artifact that causes waves to spread in time and/or space, much like material dispersion in optical systems. A fully functional FDTD implementation was first created by Yee [44] in 1966. This successful FDTD algorithm, known as Yee's Algorithm goes as follows: 1) Discretize the domain 2) Implement typical finite difference approximations to partial derivatives, but stagger $\mathbf{E}$ and $\mathbf{H}$ fields between calculation points (see Figure A.3) 3) Solve stagged field finite difference equations at every time step (see equations below specifically for one-dimensional spatial systems).

$$\mathbf{E}_{\mathbf{x}}^{\mathbf{t+\Delta t}} = \mathbf{E}_{\mathbf{x}}^{\mathbf{t}} + \frac{\mathbf{\Delta t}}{\epsilon \mathbf{\Delta x}} \left(\mathbf{H}_{\mathbf{x+1/2\Delta x}}^{\mathbf{t+1/2\Delta t}} - \mathbf{H}_{\mathbf{x-1/2\Delta x}}^{\mathbf{t+1/2\Delta t}} \right) \tag{A.11}$$

$$\mathbf{H}_{\mathbf{x+1/2\Delta x}}^{\mathbf{t+1/2\Delta t}} = \mathbf{H}_{\mathbf{x+1/2\Delta x}}^{\mathbf{t-1/2\Delta t}} + \frac{\mathbf{\Delta t}}{\mu \mathbf{\Delta x}} \left(\mathbf{E}_{\mathbf{x+\Delta x}}^{\mathbf{t}} - \mathbf{E}_{\mathbf{x}}^{\mathbf{t}} \right) \tag{A.12}$$

In Figure A.3 and equations above, the magnetic field is calculated at points every half integer, where as the electric field is calculated at every integer. This successfully produces the stagger needed for Yee Algorithm. Also, in the equations, ϵ and μ contains the wave propagation medium material definitions throughout the time-domain and spatial domains. More complex material definitions or empirical material properties may require further approximation of approximation manipulation to yield

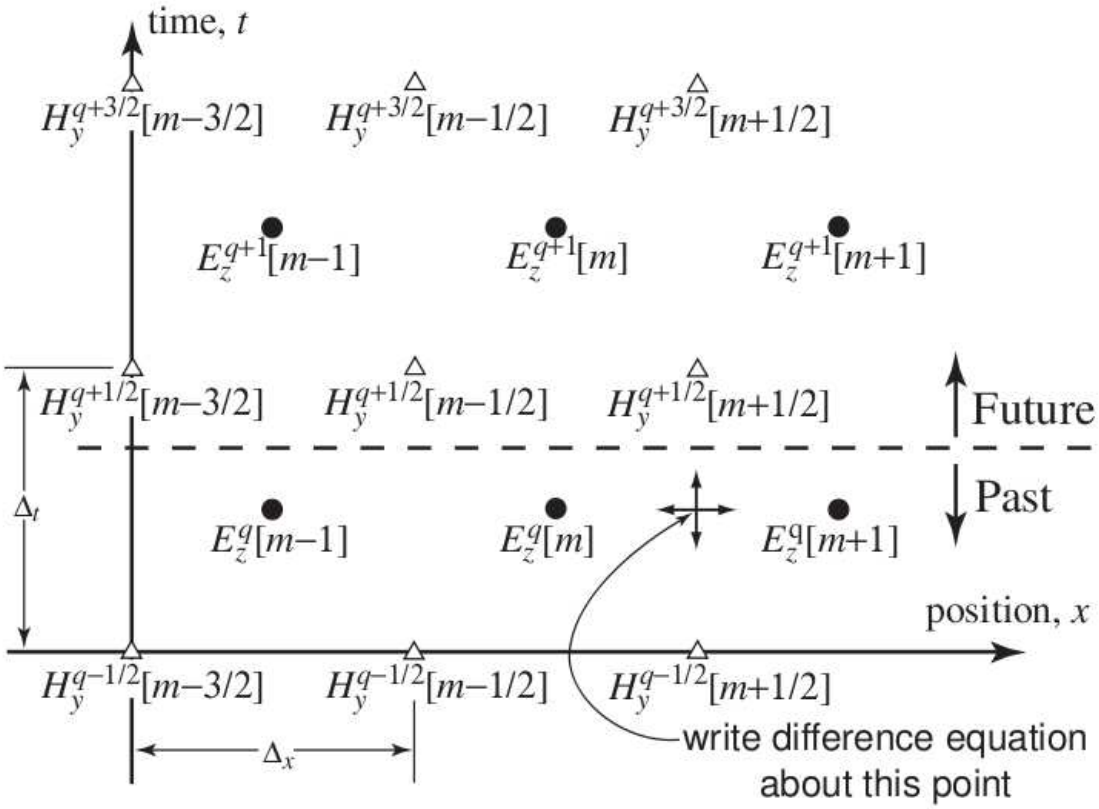

Figure A.3: The domain discretization is shown for a two-dimensional implementation of Yee's Algorithm in FDTD calculation. Here, the electric field and magnetic field points are staggered both in the spatial x-axis and time t-axis to prevent numerical dispersion. Future time points are calculated from past time spatial points using the finite difference method technique. The figure was borrowed from Chapter 3 in [45].

a suitable form. This concludes the brief introduction of FDTD. Approximations to the Maxwell Equations using the FDTD method is an easy, yet robust approximation scheme to be used in the calculation of complex electrodynamic models. It is noted that further information is needed to fully implement these approximations in specific cases. In particular, convergence and stability criterion were not discussed, since it was not relevant for this introduction. From here, the following references are particularly useful for further development of FDTD methodology and practice [45].

A.1.3 FDTD Terminating Boundary Considerations

One item that was not discussed in the development of FDTD in the above section was the issue wave propagation through finite domain media. In nature and in the lab, light emitted from a source, whether it be the Sun, a light bulb, or a laser, eventually is absorbed or scattered by the surrounding environment. Similarity, in the computational environment, an effective absorber is necessary to eliminate wave propagation at the ends of the finite spatial domain. Imperfect absorbers cause unwanted reflections which are returned into the simulation environment creating errors. Therefore, the need for perfect numerical wave absorbers are necessary to efficiently computation and accurate characterization of complex electrodynamic systems in numerical FDTD. Here, a brief introduction to absorbing boundaries in FDTD systems is presented.

There are several methods in FDTD for terminating a domain at its boundary. For the purposes of this brief introduction, only two are covered due to the authors familiarity. The first terminating boundary condition is knowns as the one-dimensional absorbing boundary condition or ABC, and is the simplest to apply to FDTD codes. The central idea of ABC is matching the electric and magnetic fields at the boundary end points with the electric and magnetic fields next to the end points. This boundary condition matches that of a vibrating string with one end of the string as a source of vibration, and the other end is loop around a pole. When the end of the string vibrates, it moves up and down the down with the vibration, instead of reflecting as would happen if it was directly attached to the pole. As an example, implemented in an 1-D FDTD code, outlay the end points of the discretized domain, and set them as the nearby calculated field values as follows.

At this point, one may wonder why there are so many absorbing boundary conditions is ABCs work so well. The simple answer is they do not work well in most FDTD problems. ABCs work very well in 1-D problems were the electric and magnetic field behave nicely. They can also work well in higher dimensional problems with some modification. However, it most computational scenarios, they do not work well, such as nonlinear problems, or light and oblique incidences to the ABC. Thus, a more robust, comprehensive approach to absorptive boundary conditions is necessary.

This leads to the second terminating boundary condition of interest as perfectly-match-layers or PML. PML is considered the sexy, "state of the art" approach to boundary conditions in FDTD codes, as it provides a general, robust solution in terminating FDTD domain end reflections. PML was proposed by J.-P. Berenger in 1994 [cite], and since then, many versions of PML with better performance have been proposed as well [cite]. The central idea behind PML is that it is a computational artificial material that is extremely lossy, or absorptive, to incident light of any frequency, incidence, etc. First, the artificial material must have the same impedance as the lossless computational domain to prevent reflections of incident light and to allow it to fully enter. Second, once light enters, it must yield to extremely absorption within.

There are many formulations of PML that exist, all with different derivations, all very effective. Instead of diving into a particular PML formulation, an FDTD simulation was run using PML as a boundary condition to demonstrate its effectiveness as an absorbing material. In Figure A.4, a single frequency wave is incident upon a layer of PML. The colors red and blue represent the electric field oscillation. For zero field, white is represented. In lossless domain, the oscillation of the single frequency wave is observed. However, in the PML layer, the fields are quickly absorbed. Thus, it is clear from this simple result that PML is very effective at absorbing light at the boundaries of FDTD computational domains.

For PML to be effective in nearly complete absorption, the thickness of PML needs to be at least half the longest wavelength used in the computation. For single frequency FDTD simulations, the PML thickness is rather easy to apply. However, for multi-frequency FDTD simulations, caution is advised in setting a PML thickness to be large enough to absorb all frequencies used. Although PML is extremely effective in terminating domain end reflections, technically speaking, PML is not really a boundary condition. Traditionally, a boundary condition is defined on a point, line or surface. Here, PML is an artificial material used for computation convenience for which it must to coat the outer edges of the computational domain to eliminates reflections of nearly all light it touches. Because of this, the computational domain must account for extra PML materials around the edges.

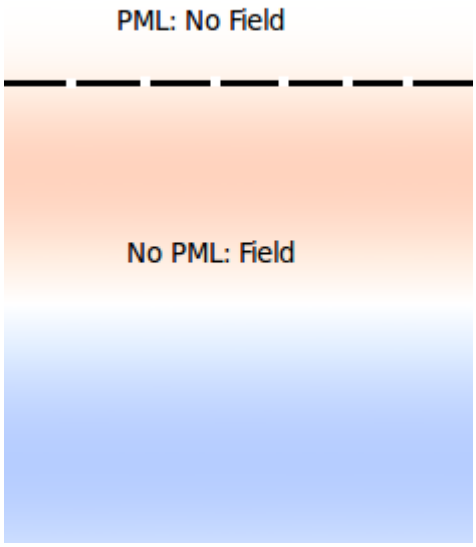

Figure A.4: Shown is a two spatial dimensional FDTD simulation utilizing PML at the top boundary. Where there is no PML, a half-wavelength of oscillating electric field is seen. However, where PML is placed, no electric field is present, thus demonstrating its near perfect absorptive effects. Through use of PML, easy, low computation FDTD simulations are possible, eliminated unusually grid patterning or large grid domains.

This concludes the brief introduction to FDTD terminating boundary conditions. For more information regarding FDTD and boundary conditions, see these references [cite].

Appendix B

Numerical Validation

General analytical calculations of nonlinear optical systems are often difficult or impossible to obtain from the Maxwell equations given the field dependence of nonlinear optical materials. Thus, numerical methods are required to calculate nonlinear systems. In this appendix, numerical considerations to nonlinear homogeneous dielectric slabs and nonlinear metal-dielectric gratings are discussed. Experiential knowledge accumulated through hundreds of numerical simulations of nonlinear systems is recorded for reference in future work related to this area. In particular, focus is given to items such as grid layout and convergence. Also, transmission spectrum are presented in validation of the numerical modeling accomplished through FDTD.

B.1 FDTD of Homogeneous Dielectric Slab

The numerical calculation of linear and nonlinear homogeneous dielectric slabs are greatly important to the topics of this thesis. Its solutions are used as a mathematical mapping from metal-dielectric gratings and as reference slabs to compare nonlinear enhancement properties. In this section, the numerical simulation of homogeneous dielectric slabs are discussed. Also, a validation of the FDTD setup are detailed using a comparison between analytical and computational solutions in transmission.

B.1.1 Grid Setup

To setup the numerical calculation for the transmission of the homogeneous dielectric slab via the FDTD method, first the domain of the system must be determined. As the name implies, a homogeneous dielectric material is assumed to have the same optical properties throughout the material in at least one direction. Thus, to determine the size of the spatial domain, only the direction of light propagation relative to the material interface is necessary. For light at normal incidence, i.e. perpendicular to the material interface, only one spatial dimension is required to fully capture the transmission characteristics of a homogeneous dielectric slab, since light is only propagating along one spatial dimension. Therefore, transmission of normal incident light through a homogeneous dielectric slab is a two-dimension domain with one spatial dimension and one time dimension. For light at an oblique incidence to a homogeneous dielectric slab, i.e. at an angle to the material interface, two spatial dimensions required to fully capture the transmission characteristics of a homogeneous dielectric slab. Even though one spatial dimension is required for the simulation of material properties, two spatial dimensions are needed to fully capture the wave propagation. Therefore, numerical calculation of transmission of oblique incident light through a homogeneous dielectric slab is a three-dimensional domain with two spatial dimension and one time dimension. For visualization purposes, Figure B.1 shows the differences between normal and oblique incidences, through which the reasoning for each systems spatial dimensionality becomes clear. It will be seen in the next section that metal-dielectric gratings will require a three-dimensional domain due to the inhomogeneity of the grating system.

After establishing the domain characteristics, the simulation of homogeneous dielectric slab for transmission of normal incident light is setup. In Figure B.2, a diagram of the proposed spatial layout is shown. Note that the thickness of the colors for grid layout in Figure B.2 do not carry any calculation points in the vertical direction, only in the horizontal; this was done to highlight changes in the setup for visualization purposes. Although the homogeneous dielectric slab has a two-dimensional domain, the spatial layout does not change with time. Hence, the spatial grid is setup to allow for a time evolution of the light.

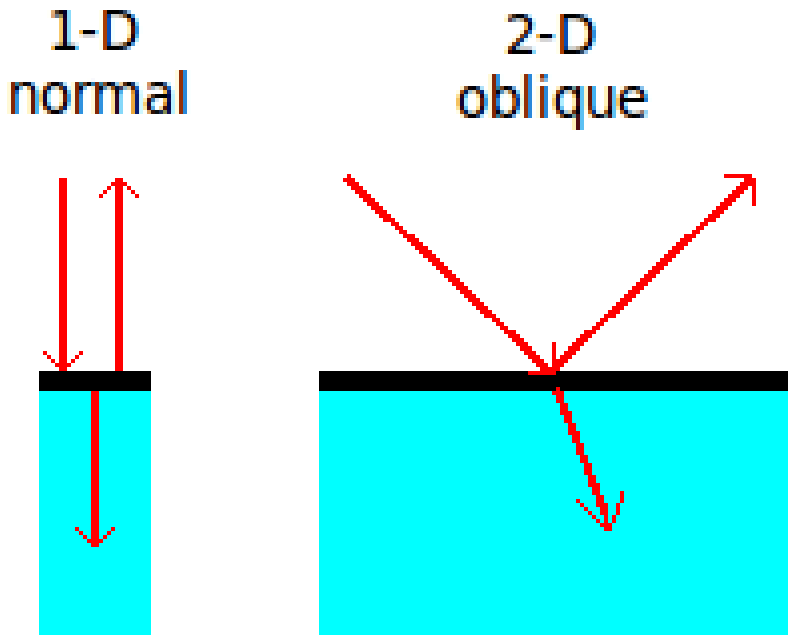

Figure B.1: Shown is the difference between normal incidence and oblique incidence. For normal incidence, only one spatial dimension is necessary to capture the light propagation. Conversely, two spatial dimensions are necessary.

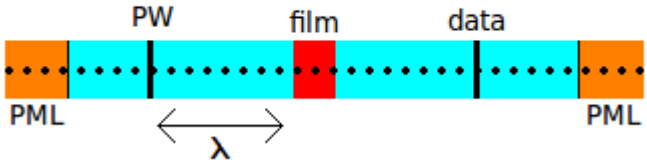

Figure B.2: Shown is a two-dimension setup for the homogeneous dielectric slab. The domain is discretized uniformly as required for the FDTD method. The homogeneous dielectric slab, red, is centered in the computational domain. A plane wave source (left) and data collection (right) was placed one wavelength away from the the dielectric film. Also, PML was placed at the ends of the computational domain to absorb transmitted and reflected light to prevent measured light reentering the computational area, as this interaction is not part of the designed simulation.

From the spatial grid layout, in Figure B.2, there is an arrangement of items within the grid that is not arbitrary, and in particular, are built around the item of interest,

in this case, a homogeneous dielectric slab. To begin, the thickness and material properties of the homogeneous dielectric slab are set. Next, the properties of source of light are determined, which are dependent upon the type of data needed. For linear spectrum calculations, finite durational Gaussian pulses are useful since they contain a ranges of frequencies. When normalized with the input pulse, it forms a complete transmission spectrum over the frequency range of interest with only two simulations. This situation provides the fastest computation, since only two computations are necessary to capture a full spectrum. Conversely, using single frequency planes waves in the calculation of transmission spectrum would require two runs per frequency of interest, resulting in many simulations to capture the full transmission spectrum. Unfortunately, for nonlinear calculations, single frequency plane-waves are the only source for calculation as nonlinear phenomena only occur for single frequencies, and broadband Gaussian pulses result in unwanted frequency mixing. Also, due to their field dependence, simulations must be ran over a range of intensities to fully capture the nonlinearity of the system.

Regardless of source type used, the location of the source is placed at least one source wavelength away from the item of interest, in this case, the homogeneous dielectric slab. In general, this is a suggested placement as it eliminates any near-field radiation interactions with the source and the item of interest, and allows the source-type to fully develops before interacting with any material. The location for data collection of electric and magnetic fields mirrors the same requirements as the source when collection radiation at the far-field. The data collection placement is at least one wavelength from the item of interest. This is required to eliminate any near field effect from the transmitted light from the material system. For homogeneous dielectric slabs, near-field effects are not an issue; however, it is good FDTD practice to place sources and data collection points at least a wavelengths distance from an significant light interaction to only gather far-field transmission.

Lastly, to eliminate reflections at the ends of the computational domain, PML, or perfectly-match-layers, a near perfect absorber of electromagnetic waves, was applied at the boundary ends. This is of critical importance to FDTD simulation as it allows for the measurement of light in complex structures without unwanted back-reflected light. As mentioned in Appendix A, this causes a great deal of problems in early FDTD simulation. For the simulation of homogeneous dielectric slabs, the execution

of PML was done as prescribed. The PML thickness was adjusted to one-half of the incident source wavelength. With the PML conditions established, it completes the grid setup for normal incidence transmission calculations of linear and nonlinear homogeneous dielectric slabs. As will be seen in the next section, the grid layout for metal-dielectric gratings is very similar, but extended into two spatial dimensions. From here, the accuracy of the FDTD setup is tested.

B.1.2 FDTD Convergence and Validation of HDS

Before computationally expensive simulations of nonlinear optical phenomena can be produced, basic tests of the FDTD simulation setup of the homogeneous dielectric slab must be performed. Several simple tests of physical quantities, such as energy conservation and field visualization, are useful to determine whether the qualitative aspects of the simulation are correct. However, the best tests of simulations come from comparison to analytical solutions. Setting up an FDTD simulation under the same assumption as a particular analytical solution should yield equivalent responses under the same inputs.

To test the accuracy of the FDTD simulation of transmission of normal incident light through a homogeneous dielectric slab, the response of the simulation was compared to the analytical solution. The analytical solution is only valid for linear optical systems, and thus obviously does not apply to nonlinear optical systems. However, nonlinear optical systems converge to linear systems when the input light intensity is at low powers. Also, validating the linear solution provides the correct foundation of exploring the nonlinear realm.

The first test of the FDTD simulation of transmission through homogeneous dielectric slab is the calculation of the transmission spectrum. In this simulation, a multi-frequency Gaussian pulse was sent through the dielectric slab. Here, only a few frequencies fully pass through the slab, as those frequencies match the propagating mode of the slab. In Figure B.3, the results of this simulation are shown. Here the horizontal axis is the normalized input frequencies and the vertical axis is the normalized transmission, with 1 representing full transmission. The FDTD simulation solution is shown as black circles, and plotted over it is the analytical solution in

red circles. Since both solutions overlap, it is clear that the FDTD simulation and analytical solution agree. Thus, the FDTD simulation of a dielectric slab passes well.

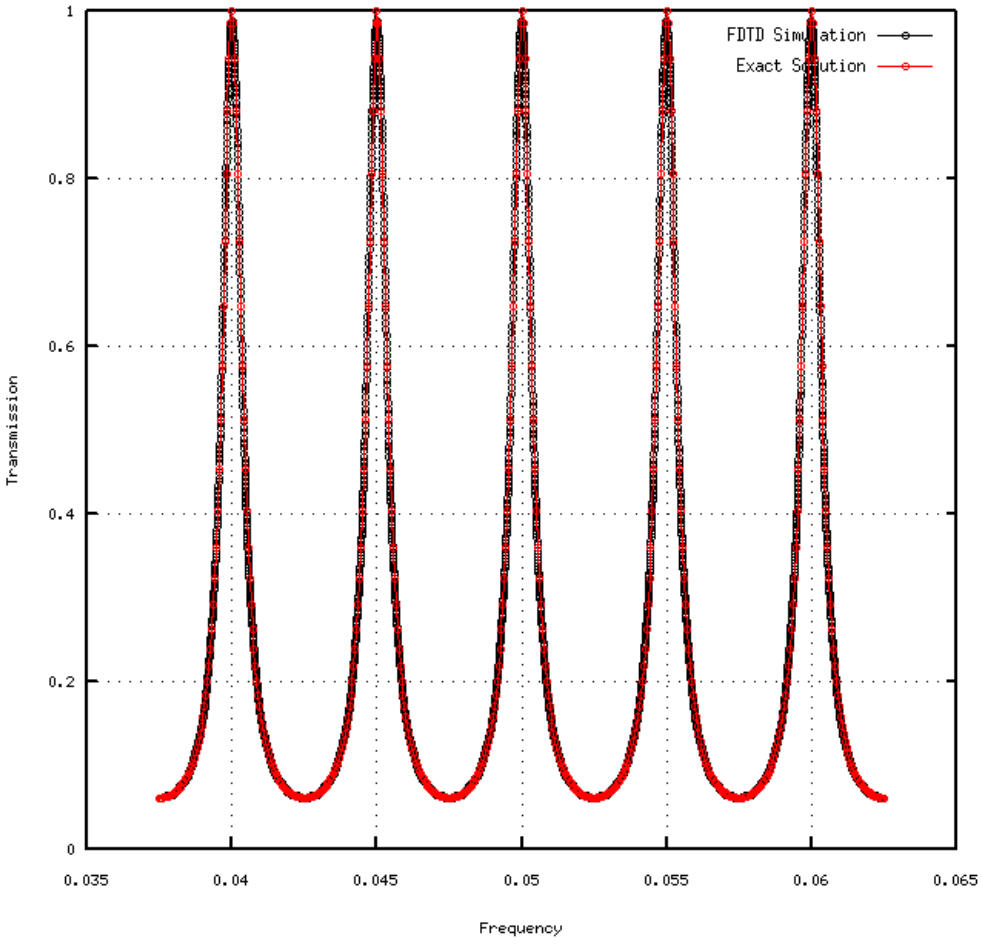

Figure B.3: Shown are the results of the homogeneous dielectric slab transmission spectrum validation. The FDTD simulation solution is shown as black circles, and the analytical solution in red circles. With both solutions overlapping, both the FDTD simulation and analytical solution agree.

Although the first test made clear that the FDTD simulation of a homogeneous dielectric slab confirms its general accuracy and its setup, it is unclear from the test how much it is in error with the analytical solution. Also unclear is how many grid points in necessary to accurately simulate the system without excess calculation. Thus, a convergence test was conducted. Specifically, this test measures the error of the dielectric slab between the FDTD simulation and analytical solution versus grid

points per wavelength used. To simplify the analysis, single-frequency plane waves were used.

In Table B.1, the results of the error and convergence test are presented. The columns are arranged by grid points, error, and time of simulation. For 200 grid points per wavelength, the FDTD simulation is nearly 10 percent in error, while only taking 2.1 s to compute. Since 10 percent error is not acceptable, the grid points per wavelength were doubled to 400. At this resolution, the error dropped to 2.4 percent error, while the time of simulation doubled to 4.2s. For further comparison, the grid points per wavelength were double again to 800. At this resolution, the error was smaller at 1.6 percent error, yet the time of simulation was nearly 12s. From this analysis, it is clearly seen that doubling of the grid points does result in lower error. However, doubling of grid points also greatly increases the time of simulation. Since the FDTD simulation of homogeneous dielectric slabs are computationally inexpensive, high resolution, low error simulation was easily achievable within seconds and minutes. Thus, only the error convergence is of concern. However, it will be seen later that FDTD simulation of metal-dielectric gratings are very computationally expensive, requiring hours or even days to run. For these cases, error compromises must be made.

Diet Resolution Error		
Points in One Wavelength	Percent Error	Time to Compute
200	9.8	2.1 s
400	2.4	4.2 s
800	1.6	11.8 s

Table B.1: Convergence of FDTD homogeneous dielectric slab. Increasing the points per wavelength resolution reduces error but also increases total time of calculation.

This concludes the FDTD convergence and validation of the transmission of normal incidence light through homogeneous dielectric slabs. From this introduction, guidance was provided in the setup of FDTD simulations of homogeneous dielectric slabs. Also, the FDTD simulation of these systems was successfully validated, error calculated, and convergence understood.

B.2 FDTD of Metal-Dielectric Gratings

The numerical calculation of linear and nonlinear metal-dielectric gratings are central to the topic of this thesis: enhancement of optical nonlinearity. Its solutions are only obtainable by numerical simulation. In this section, the numerical simulation of metal-dielectric gratings are discussed. Also, a validation of the FDTD setup are detailed using a comparison between analytical and computational solutions in transmission.

B.2.1 Grid Layout

To setup the numerical calculation for the transmission of metal-dielectric gratings via the FDTD method, first the domain of the system must be determined. Since the material is inhomogeneous, the spatial domain is required to have two spatial dimensions, even when the light is at normal incidence to the film interface. Therefore, transmission of normal incident light through a metal-dielectric grating is a three-dimension domain with two spatial dimensions and one time dimension. In the case of light at an oblique incidence to a metal-dielectric grating two spatial dimensions are still required to fully capture the transmission characteristics. After establishing the domain characteristics, the simulation of metal-dielectric gratings for transmission of normal incident light is setup. In Figure B.4, a diagram of the proposed spatial layout is shown.

To start, the metal-dielectric grating was placed in the center of the domain with its necessary material definitions applied. Here, the MD grating runs along the center of the horizontal axis. Similarly to the FDTD simulation of the homogeneous dielectric slab, PML layers were placed at the top and bottom the computational domain to absorb transmitted and reflected light from the grating. Also, source light and data collection was placed one wavelength from the grating to allow the source radiation to fully develop and avoid near-field data collection as only the far-field was of interest. Although the MD grating has a three-dimensional domain, the spatial layout does not change with time. Hence, the spatial grid is setup to allow for a time evolution of the light.

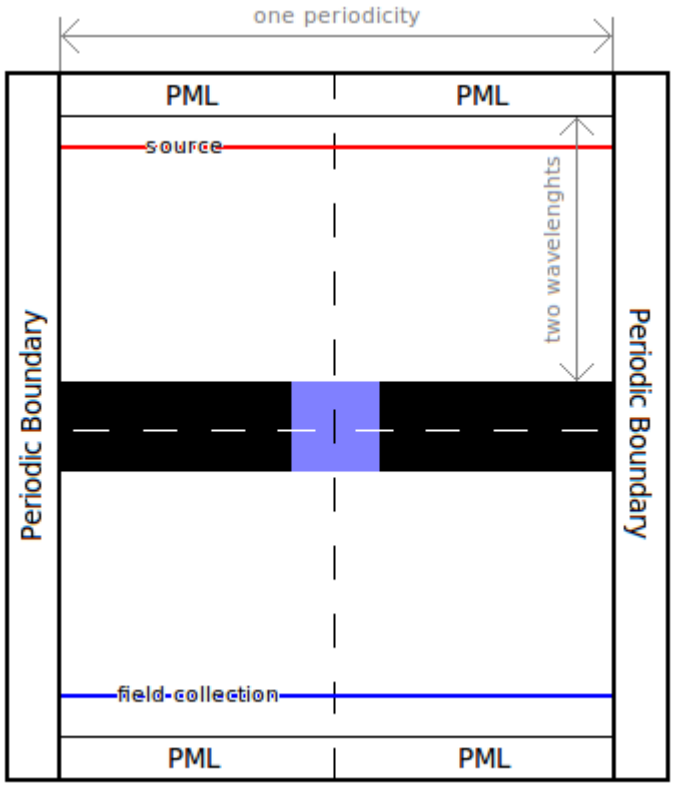

Figure B.4: Shown is a three-dimension setup for the metal-dielectric grating. The domain is is discretized uniformly as required for the FDTD method. One periodicity is only needed for full simulation, and is centered in the computational domain. A plane wave source (top) and data collection (bottom) was placed one wavelength away from the the grating. Also, PML was placed at the ends of the computational domain to absorb transmitted and reflected light to prevent measured light reentering the computational area, as this interaction is not part of the designed simulation. Furthermore, a periodic boundary condition was placed on the sides of the computational domain to reduce the size to one periodicity. Lastly, a symmetry condition was applied around the vertical axis to further reduce the computation domain by half.

By using the unit cell of the metal-dielectric grating, the FDTD simulation can be very efficient. Although the analysis of MD gratings assumes that it infinite is length, only one periodicity is necessary to simulate. Using a periodic boundary conditions on the left and right sides of the domain properly captures this infinity assumption. Also, it eliminated a larger computational domain containing multiple grating periodicities. Furthermore, this limits the width of the computational domain to the size of the unit cell, being one periodicity. Since the unit cell of the MD grating

is symmetrical, by placing the dielectric slit in the center, a symmetry condition was applied along the central vertical axis to reduce computational work by half. Through this specific layout for the metal-dielectric grating, the FDTD simulation is fully optimized for computational efficiency. This completes the grid setup for normal incidence transmission calculations of linear and nonlinear metal-dielectric gratings.

B.2.2 FDTD Convergence and Validation of MDG

Before computationally expensive simulations of nonlinear optical phenomena can be produced, basic tests of the FDTD simulation setup of the metal-dielectric grating must be performed. Several simple tests of physical quantities, such as energy conservation and field visualization, are useful to determine whether the qualitative aspects of the simulation are correct. However, the best tests of simulations come from comparison analytical solutions. Setting up an FDTD simulation under the same assumption as a particular analytical solution should yield equivalent responses under the same inputs.

To test the accuracy of the FDTD simulation of transmission of normal incident light through a metal-dielectric grating, the response of the simulation was compared to the analytical solution. The analytical solution is only valid for linear optical systems, and thus obviously does not apply to nonlinear optical systems. However, nonlinear optical system converge to linear systems when the input light intensity is at low powers. Also, validating the linear solution provides the correct foundation of exploring the nonlinear realm.

The first test of the FDTD simulation of transmission through metal-dielectric gratings is the calculation of the transmission spectrum. In this simulation, a multi-frequency Gaussian pulse was sent through the dielectric slab. Here, only a few frequencies fully pass through the slab, as those frequencies match the propagating mode of the slab. In Figure B.5, the results of this simulation are shown. Here the horizontal axis is the normalized input frequencies and the vertical axis is the normalized transmission, with 1 representing full transmission. The FDTD simulation solution is shown as black circles, and plotted over it is the analytical solution in red circles. Since both solutions overlap, it is clear that the FDTD simulation and

analytical solution agree. Thus, the FDTD simulation of a metal-dielectric grating passes well.

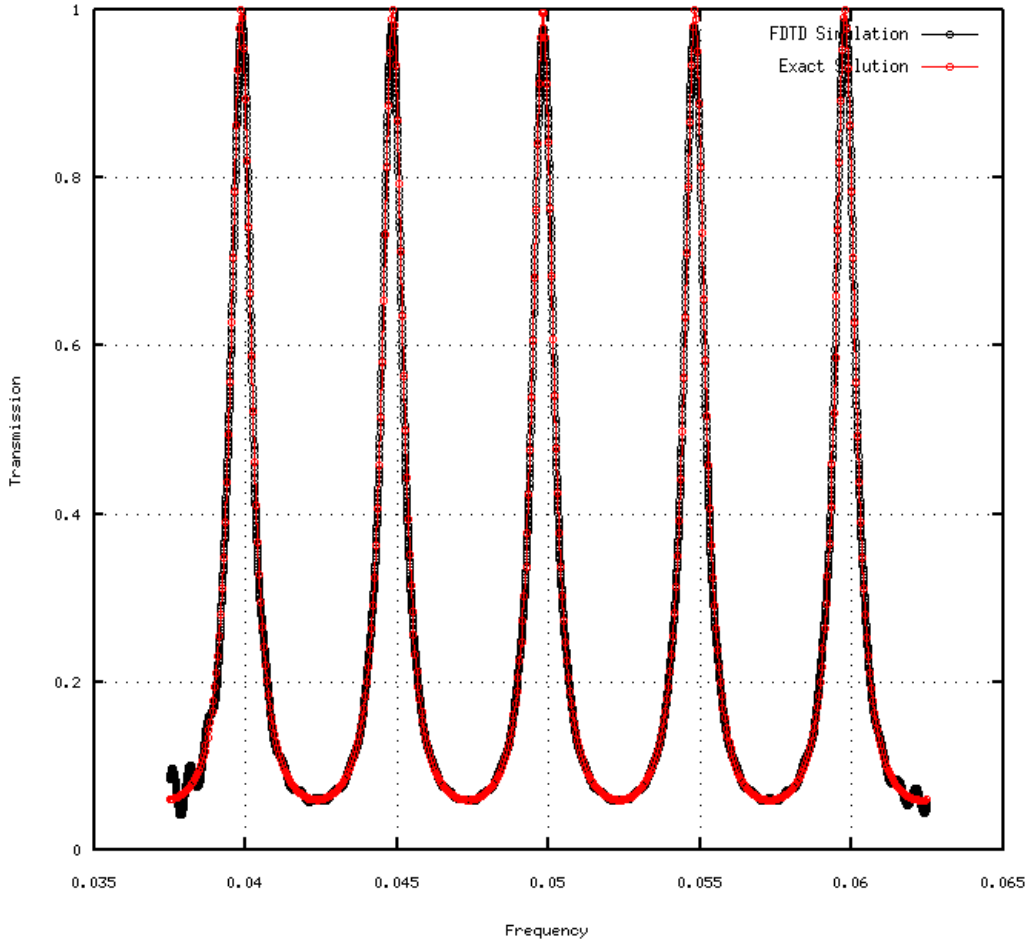

Figure B.5: Shown are the results of the metal-dielectric transmission spectrum validation. The FDTD simulation solution is shown as black circles, and the analytical solution in red circles. With both solutions overlapping, both the FDTD simulation and analytical solution agree.

Although the first test made clear that the FDTD simulation of a metal-dielectric grating confirms its general accuracy and its setup, it is unclear from the test how much it is in error with the analytical solution. Also unclear is how many grid points in necessary to accurately simulate the system without excess calculation. Thus, a convergence test was conducted. Specifically, this test measures the error of the metal-dielectric grating between the FDTD simulation and analytical solution versus

grid points per wavelength used. To simplify the analysis, single-frequency plane waves were used.

In Table B.2, the results of the error and convergence test are presented. The columns are arranged by grid points, error, and time of simulation. For 200 grid points per wavelength, the FDTD simulation is 4.6 in error, while only taking 14.5 s to compute. Since 4.6 percent error is not acceptable, the grid points per wavelength were doubled to 400. At this resolution, the error dropped to 0.60 percent error, an acceptable error, while the time of simulation ballooned to 109s. For further comparison, the grid points per wavelength were double again to 800. At this resolution, the error was smaller at 0.48 percent error, yet the time of simulation ballooned further to 1379s, over twenty minutes. From this analysis, it is clearly seen that doubling of the grid points does result in lower error. However, doubling of grid points also greatly increases the time of simulation.

MD Grating Resolution Error		
Points in One Wavelength	Percent Error	Time to Compute
200	4.60	14.5 s
400	0.60	109 s
800	0.48	1379 s

Table B.2: Convergence of FDTD metal-dielectric slab. Increasing the points per wavelength resolution reduces error but also increases total time of calculation.

From the results of Table B.2, it may suggest to be happy 0.60 percent error with the 400 grid points per wavelength resolution, and forget about higher resolutions since they require longer run time. However, this error is only for linear solutions, as its error was compared to the analytical solution. When using resolutions like 400 in nonlinear simulations of metal-dielectric gratings, the linear parts was in low error, but the nonlinear parts are in large error, as seen in Table B.3.

Here, these nonlinear errors arise from differences in the PEC metal assumption and grid domain as seen in Figure B.3. The discretization in the slit generates a gap between the last grid point in the slit and the grid point in the PEC metal. Since the fields do not enter the metal, the last grid point next to the metal wall becomes the effective slit width. Therefore, this numerical reduction of slit width results in a small field error of linear calculations, but large error for nonlinear calculations as

this error is cubic for second-order nonlinear materials and quartic for third-order nonlinear materials.

For example, take the 400 grid points per wavelength case which generated a linear error of 0.6 percent. For a grating geometry of $\lambda/d = 10$ and $d/a = 4$, a standard grating in this thesis, there are only 10 points in the slit. Using the error calculations from Table B.3, it is seen that the numerical slit reduction effect generates a minimum nonlinear error of 56 percent in second-order nonlinear systems and 95 percent in third-order nonlinear systems. Therefore, to properly model nonlinear metal-dielectric gratings at subwavelength scales, large grid points per wavelength are necessary, roughly 3200 (8x larger), to yield nonlinear errors less than 10 percent. It is worth noting that these nonlinear errors are specific to metal-dielectric gratings, as the inhomogeneity between the metal and dielectric materials in the grating structure generate the error, and does not apply to the nonlinear computation of the homogeneous dielectric slab.

NL Minimum Error		
Points in Slit	2nd-Order Error	3rd-Order Error
10	56.3	95.3
20	23.5	37.2
30	14.8	23.0
40	10.8	16.6
60	7.0	10.7
80	5.2	7.9
200	2.0	3.1
640	0.6	0.9

Table B.3: Nonlinear convergence in metal-dielectric gratings. Where linear errors convergence nicely at 20 points in the slit, nonlinear errors remain very large.

This concludes the FDTD convergence and validation of the transmission of normal incidence light through metal-dielectric gratings. From this introduction, guidance was provided in the setup of FDTD simulations of metal-dielectric gratings. Also, the FDTD simulation of these systems was successfully validated, error calculated, and convergence understood. Furthermore, nonlinear errors specific to metal-dielectric gratings were quantified.

References

[1] J. A. Porto, L. Martín-Moreno, and F. J. García-Vidal. Optical bistability in subwavelength slit apertures containing nonlinear media. *Phys. Rev. B*, 70(8):081402, Aug 2004.

[2] Yongmin Liu, Guy Bartal, Dentcho A. Genov, and Xiang Zhang. Subwavelength discrete solitons in nonlinear metamaterials. *Phys. Rev. Lett.*, 99(15):153901, Oct 2007.

[3] Changjun Min, Pei Wang, Chunchong Chen, Yan Deng, Yonghua Lu, Hai Ming, Tingyin Ning, Yueliang Zhou, and Guozhen Yang. All-optical switching in subwavelength metallic grating structure containing nonlinear optical materials. *Opt. Lett.*, 33(8):869–871, Apr 2008.

[4] J. A. H. van Nieuwstadt, M. Sandtke, R. H. Harmsen, F. B. Segerink, J. C. Prangsma, S. Enoch, and L. Kuipers. Strong modification of the nonlinear optical response of metallic subwavelength hole arrays. *Phys. Rev. Lett.*, 97(14):146102, Oct 2006.

[5] Bahaa E. A. Saleh and Malvin Carl Teich. *Nonlinear Optics*, pages 737–798. John Wiley Sons, Inc., 2001.

[6] Weber. *Handbook of Optical Materials*, pages 737–798. CRC Press, 2001.

[7] G. D. Miller, R. G. Batchko, W. M. Tulloch, D. R. Weise, M. M. Fejer, and R. L. Byer. 42%-efficient single-pass cw second-harmonic generation in periodically poled lithium niobate. *Opt. Lett.*, 22(24):1834–1836, Dec 1997.

[8] H.M. Gibbs. *Optical bistability: controlling light with light*. Quantum electronics–principles and applications. Academic Press, 1985.

[9] Tarek S. El-Bawab. Optical switching in communications networks. In Tarek S. El-Bawab, editor, *Optical Switching*, pages 333–379. Springer US, 2006.

[10] DIMITRI A. PARTHENOPOULOS and PETER M. RENTZEPIS. Three-dimensional optical storage memory. *Science*, 245(4920):843–845, 1989.

[11] M. Takenaka, M. Raburn, and Y. Nakano. All-optical flip-flop multimode interference bistable laser diode. *Photonics Technology Letters, IEEE*, 17(5):968 –970, may 2005.

[12] Katia Gallo, Gaetano Assanto, Krishnan R. Parameswaran, and Martin M. Fejer. All-optical diode in a periodically poled lithium niobate waveguide. *Applied Physics Letters*, 79(3):314–316, 2001.

[13] M. Yamada, N. Nada, M. Saitoh, and K. Watanabe. First-order quasi-phase matched linbo3 waveguide periodically poled by applying an external field for efficient blue second-harmonic generation. *Applied Physics Letters*, 62(5):435 –436, feb 1993.

[14] C. K. Chen, T. F. Heinz, D. Ricard, and Y. R. Shen. Detection of molecular monolayers by optical second-harmonic generation. *Phys. Rev. Lett.*, 46:1010–1012, Apr 1981.

[15] Kodo Kawase, Yuichi Ogawa, Yuuki Watanabe, and Hiroyuki Inoue. Non-destructive terahertz imaging of illicit drugs using spectral fingerprints. *Opt. Express*, 11(20):2549–2554, Oct 2003.

[16] D.M. Mittleman, M. Gupta, R. Neelamani, R.G. Baraniuk, J.V. Rudd, and M. Koch. Recent advances in terahertz imaging. *Applied Physics B: Lasers and Optics*, 68:1085–1094, 1999.

[17] R.M. Woodward, V.P. Wallace, D.D. Arnone, E.H. Linfield, and M. Pepper. Terahertz pulsed imaging of skin cancer in the time and frequency domain. *Journal of Biological Physics*, 29:257–259, 2003.

[18] Wenjiang Nie. Optical nonlinearity:phenomena, applications, and materials. *Advanced Materials*, 5(7-8):520–545, 1993.

[19] C. Sauteret, J. P. Hermann, R. Frey, F. Pradère, J. Ducuing, R. H. Baughman, and R. R. Chance. Optical nonlinearities in one-dimensional-conjugated polymer crystals. *Phys. Rev. Lett.*, 36:1162–1162, May 1976.

[20] J. L. Oudar. Optical nonlinearities of conjugated molecules. stilbene derivatives and highly polar aromatic compounds. *The Journal of Chemical Physics*, 67(2):446–457, 1977.

[21] Michael L. Steigerwald and Louis E. Brus. Semiconductor crystallites: a class of large molecules. *Accounts of Chemical Research*, 23(6):183–188, 1990.

[22] S. Schmitt-Rink, D. S. Chemla, and D. A. B. Miller. Theory of transient excitonic optical nonlinearities in semiconductor quantum-well structures. *Phys. Rev. B*, 32:6601–6609, Nov 1985.

[23] Eiichi Hanamura. Very large optical nonlinearity of semiconductor microcrystallites. *Phys. Rev. B*, 37:1273–1279, Jan 1988.

[24] D. Shen. Picosecond optical bistability in ZnSe-ZnTe/CaF2 multiple quantum wells at room temperature. *Journal of Crystal Growth*, 117:519–522, February 1992.

[25] H. C. Chui, G. L. Woods, M. M. Fejer, E. L. Martinet, and Jr. J. S. Harris. Tunable mid-infrared generation by difference frequency mixing of diode laser wavelengths in intersubband ingaas/alas quantum wells. *Applied Physics Letters*, 66(3):265–267, 1995.

[26] A. E. Neeves and M. H. Birnboim. Composite structures for the enhancement of nonlinear-optical susceptibility. *J. Opt. Soc. Am. B*, 6(4):787–796, Apr 1989.

[27] R. H. Magruder, R. F. Haglund, L. Yang, J. E. Wittig, and R. A. Zuhr. Physical and optical properties of Cu nanoclusters fabricated by ion implantation in fused silica. *Journal of Applied Physics*, 76:708–715, July 1994.

[28] K. Uchida, S. Kaneko, S. Omi, C. Hata, H. Tanji, Y. Asahara, A. J. Ikushima, T. Tokizaki, and A. Nakamura. Optical nonlinearities of a high concentration of small metal particles dispersed in glass: copper and silver particles. *J. Opt. Soc. Am. B*, 11(7):1236–1243, Jul 1994.

[29] H. B. Liao, R. F. Xiao, H. Wang, K. S. Wong, and G. K. L. Wong. Large third-order optical nonlinearity in Au:TiO2 composite films measured on a femtosecond time scale. *Applied Physics Letters*, 72:1817, April 1998.

[30] Junji Yumoto, Seiji Fukushima, and Ken ichi Kubodera. Observation of optical bistability in cdsxse1-x-doped glasses with 25-psec switching time. *Opt. Lett.*, 12(10):832–834, Oct 1987.

[31] H. M. Gibbs, S. L. McCall, and T. N. C. Venkatesan. Differential gain and bistability using a sodium-filled fabry-perot interferometer. *Phys. Rev. Lett.*, 36:1135–1138, May 1976.

[32] Luigi Scaccabarozzi, M. M. Fejer, Yijie Huo, Shanhui Fan, Xiaojun Yu, and James S. Harris. Enhanced second-harmonic generation in algaas/alxoy tightly confining waveguides and resonant cavities. *Opt. Lett.*, 31(24):3626–3628, Dec 2006.

[33] Vilson R. Almeida and Michal Lipson. Optical bistability on a silicon chip. *Opt. Lett.*, 29(20):2387–2389, Oct 2004.

[34] Takasumi Tanabe, Masaya Notomi, Satoshi Mitsugi, Akihiko Shinya, and Eiichi Kuramochi. Fast bistable all-optical switch and memory on a silicon photonic crystal on-chip. *Opt. Lett.*, 30(19):2575–2577, Oct 2005.

[35] Zhenshan Yang, Philip Chak, Alan D. Bristow, Henry M. van Driel, Rajiv Iyer, J. Stewart Aitchison, Arthur L. Smirl, and J. E. Sipe. Enhanced second-harmonic generation in algaas microring resonators. *Opt. Lett.*, 32(7):826–828, Apr 2007.

[36] P. P. Absil, J. V. Hryniewicz, B. E. Little, P. S. Cho, R. A. Wilson, L. G. Joneckis, and P.-T. Ho. Wavelength conversion in gaas micro-ring resonators. *Opt. Lett.*, 25(8):554–556, Apr 2000.

[37] J. T. Shen, Peter B. Catrysse, and Shanhui Fan. Mechanism for designing metallic metamaterials with a high index of refraction. *Phys. Rev. Lett.*, 94(19):197401, May 2005.

[38] Jonghwa Shin, Jung-Tsung Shen, Peter B. Catrysse, and Shanhui Fan. Cut-through metal slit array as an anisotropic metamaterial film. *Selected Topics in Quantum Electronics, IEEE Journal of*, 12(6):1116 –1122, nov.-dec. 2006.

[39] J. T. Shen and P. M. Platzman. Properties of a one-dimensional metallophotonic crystal. *Phys. Rev. B*, 70(3):035101, Jul 2004.

[40] Ardavan F. Oskooi, David Roundy, Mihai Ibanescu, Peter Bermel, J. D. Joannopoulos, and Steven G. Johnson. MEEP: A flexible free-software package for electromagnetic simulations by the FDTD method. *Computer Physics Communications*, 181:687–702, January 2010.

[41] David L Powers. Boundary value problems / david l. powers. 1979.

[42] T J R Hughes. *The Finite Element Method: Linear Static and Dynamic Finite Element Analysis*, volume 682. Dover Publications, 2000.

[43] A. Taflove and S.C. Hagness. *Computational electrodynamics: the finite-difference time-domain method*. Artech House antennas and propagation library. Artech House, 2005.

[44] Kane Yee. Numerical solution of initial boundary value problems involving maxwell's equations in isotropic media. *Antennas and Propagation, IEEE Transactions on*, 14(3):302 –307, may 1966.

[45] John B. Schneider. *Understanding the Finite-Difference Time-Domain Method.*

[46] Marin Soljačić, Mihai Ibanescu, Steven G. Johnson, Yoel Fink, and J. D. Joannopoulos. Optimal bistable switching in nonlinear photonic crystals. *Phys. Rev. E*, 66(5):055601, Nov 2002.

Vita

Daniel J. Ironside

7546 Byron Pl. Apt 3S
St. Louis, MO 63105

Phone: (314) 496-5960
Email: daniel.j.ironside@gmail.com

Education

- **M.S. Electrical Engineering**, Washington University in St. Louis, May 2012
  - GPA: 3.93/4.00
- **B.S. Aerospace Engineering, Mathematics**, Saint Louis University (SLU), May 2010
  - GPA: 3.98/4.00, *Summa Cum Laude*
- **B.S. Physics**, Saint Louis University, May 2010
  - GPA: 3.98/4.00, *Summa Cum Laude*

Industry Experience

- **Student Engineer**, The Boeing Company, Houston, TX, May 2008 - Aug. 2009

  • Developed & validated a mathematical and physical model of the composite mass properties of the on-orbit mated International Space Station, the Space Shuttle, and the payload grappled Space Station Robotic Arm. This tool was used for joint Space Shuttle/Space Station Flight Control and GN&C analysis; and was especially important since its results were programmed into Space Shuttle flight control software and updated per mission. The software was developed in Matlab and contained an easy-to-use input GUI which including an accurate orientation model of the Shuttle, Station, payload grappled Robotic Arm for visualization and validation purposes. Due to the importance and rapid development of this project, I was awarded a Pride@Boeing Accomplishment

Award for my work.

• Responsible for real-time mission support of Space Shuttle missions STS-124, STS-127 in the Mission Evaluation Room at NASA-Johnson Space Center. This included pre/post-mission data analysis that compared the real flight data with the prediction models from our team.

• Analyzed the structural dynamic modes & deflections of a payload grappled Space Shuttle Robotic Arm under Space Shuttle control jet firings. This tool was developed and validated for the last Space Shuttle mission to the Hubble Space Telescope, STS-125.

• Participated in Boeing Space Exploration Intern 2009 Y-Prize Competition. Under competition rules, we presented our design and business plan for innovation of commercial human space flight to Boeing technical fellows and business leadership. Under my guidance as technical lead, our team placed first in the competition and was awarded a Pride@Boeing Achievement Award for our work.

- **Student Engineer**, NASA-Stennis Space Center, MS, June - Aug. 2007

  • Cataloged NASA, DoD, and private sector rocket test stand facility capabilities as part of joint NASA-DoD initiative. I presented the project results to head NASA and DoD officials.

  • Developed and programmed a NASA-wide rocket test stand facility risk life-cycle management system. Users entered fixed and tracked risk information via secure webpages to Microsoft Access where NASA rocket propulsion test management could analyze rocket test stand risks.

Research Experience

- **Graduate Research Assistant**, Washington University in St. Louis, June 2010 - Present

  • Investigated new and novel electromagnetic devices focusing on metamaterials from the RF to mid-infrared frequency range. Through my research in this area, I developed robust mathematical and physical electrodynamic and RF models in the design and analysis of many metamaterial devices. The electrodynamic and RF simulation supported the interaction of real metal and dielectric materials, including dispersive, absorptive, and nonlinear properties with a wide array of radiative sources.

• Results from my EM and RF simulations were analyzed using signal processing tools I developed in Matlab to isolate specific signals.

• Due to the computation loads associate with high-fidelity, robust programs, I setup my simulations to support parallel processing on supercomputer platforms. This greatly reduced the computation time of the simulations processed.

- **Undergraduate Research Assistant**, Saint Louis University, Jan. 2008 - May 2010

  • Created a mathematical and physical structural dynamic model of an aircraft wing in coupled bending and torsion. This simulation was written in both C++ and Matlab; and was integrated with an outside aerodynamic code. This research was important to the study of unmanned aerial vehicles, as aeroelastic tailoring of aerodynamic and structural dynamic interactions results in large drag reductions, upward to 25 percent, which allows for fuel savings and increased flight range. My research efforts resulted in two conference proceedings at the AIAA Applied Aerodynamics Conference in 2008 and 2010.

Teaching Experience

- **Graduate Teaching Fellow**, NSF GK-12 Program, Aug. 2010 - May 2011
  Anthony Thomas, University City High School, MO

  • Designed year long module on aerospace engineering for high school juniors in physics to inspire students to continue to higher education in a science, technology, engineering, or mathematics (STEM) field.

  • Coordinated engineering lessons with class teacher to complement physics lessons.

  • Instructed five classes weekly; assessed and graded student performance.

- **Lab Teaching Assistant**, Engineering Physics I & II Laboratory, Aug.2008 - May 2010
  John C. James, Department of Physics, Saint Louis University

  • Instructed physics students on the experimental methods & techniques of classical mechanics, electricity & magnetism, circuits, & optics.

  • Demonstrated and assisted weekly physics lab experiments; graded weekly lab reports.

- **Undergraduate Teaching Assistant**, Freshman Engineering I, Aug. 2007 - Dec. 2007
  Shirdar Condoor, Department of Aerospace & Mechanical Engineering, Saint Louis University
  • Instructed engineering students in simple drafting techniques & Pro/Engineer software; graded homework assignments.

Journal Publications

- Ironside, D. J., Shen, J. T. "Orders of Magnitude Enhancement of Optical Nonlinearity in Subwavelength Metal-Dielectric Gratings." December 2011. *Recently Submitted.*

Conference Proceedings

- Ironside, D. J., Bramesfeld, G., and Schwochow, J. "Modeling of Wing Drag Reductions due to Structural Dynamics in Atmospheric Gusts." *AIAA Applied Aerodynamics Conference, Chicago, IL*, June 2010.
- Ironside, D. J. "The Structural Dynamics of Aircraft Wings in Bending and Torsion." *AIAA Region V Student Paper Conference, Twin Cities, MN*, April 2009.
- Bramesfeld, G., Ironside, D. J., and Schwochow, J. "Simplified Modeling of Wing-Drag Reduction due to Structural Dynamics and Atmospheric Gusts." *AIAA Applied Aerodynamics Conference, Honolulu, HI*, August 2008, (AIAA 2008-6238).

Presentations

- "Mixed-Content Friedmann-Walker-Robertson Universes" Dept. of Physics, Saint Louis University, St. Louis, MO, May, 2010.
- "Mixed-Content Friedmann-Walker-Robertson Universes" (Poster) St. Louis Area Undergraduate Research Symposium, St. Louis, MO, May 2010.

- "The Structural Dynamics of Aircraft Wings in Bending" (Poster) St. Louis Area Undergraduate Research Symposium, St. Louis, MO, April 2009. ***Won** 2^{nd} **Place**
- "The Structural Dynamics of an Aircraft Wing-Like Cantilever Beam" (Poster) Sigma Xi Research Symposium, Saint Louis University, St. Louis, MO, February 2009. ***Won** 1^{st} **Place**
- "The RPT Program Risk Life-Cycle Information Management System" NASA-USRP Student Summer Research Presentations, Stennis Space Center, MS, August 2007.

Grants & Fellowships

- NSF Graduate Research Fellowship, April 2011 – Present ***National Award**
- MIT Lincoln Laboratory Fellowship, October 2011 – April 2012
- NSF GK12 Fellowship, June 2010 – May 2011
- "Experimental Verification of Structural Dynamics and Aerodynamic Interaction in Gliders" Grants in Aid of Research, January 2010, $791

Academic Honors

- Dean's List, all semesters
- James I. Shannon Physics Award, Saint Louis University, 2010
- Sigma Xi, Saint Louis University, 2009
- Tau Beta Pi, Saint Louis University, 2008
- Pi Mu Epsilon, Saint Louis University, 2008
- Excellence in Mathematics Award, Saint Louis University, 2007
- Illinois State Scholar, 2005

Scholarship Awards

- Norbert and Santhe Scholarship, Saint Louis University, 2009
- Peter and Barbara Jackalus Scholarship, 2009
- PepsiCo Foundation Scholarship, 2008, 2009 ***National Award**
- AIAA Next Century of Flight Scholarship, 2009 ***National Award**
- Francis Regan Scholarship Award in Mathematics, 2008, 2009
- Roland Quest Memorial Scholarship Award, 2008
- Dr. Bellur Nagabhushan Endowed Scholarship, 2008
- AIAA Sam F. Iacobellis Scholarship, 2008 ***National Award**
- Donald and Nora Manahan Scholarship Award, 2008
- Boeing BOLD Scholarship for Multidisciplinary Leadership, 2006, 2007
- Parks College Book Fund Scholarship, 2007
- Dean's Scholarship, Saint Louis University, 2005-2009

Awards

- Pride@Boeing Achievement Award for 1st Place in Boeing Y-Prize Competition, 2009
- 2nd Place for Poster Presentation at St. Louis Area Undergraduate Research Symposium, 2009
- Best Undergraduate Presentation, SLU Sigma XI Research Symposium, 2009
- Pride@Boeing Accomplishment Award for MASSPROP SSRMS Development, 2008
- SAE AeroDesign East Competition, 3rd Place Overall, Micro Class, 2007
- SAE AeroDesign East Competition, 2nd Place Most Payload Lifted, Micro Class, 2007

- SAE AeroDesign West Competition, 2nd Place Overall, Open Class, 2007
- SAE AeroDesign West Competition, Most Innovative Design, Open Class, 2007

Leadership

- Students for the Exploration and Development of Space, SLU Chapter
  - • **President**, March 2007 - April 2008; **Vice-President**, May 2006 - March 2007
  - • Chartered organization in SLU Student Government Association
  - • Built group from 4 to 25+ regular members; Established bi-weekly meetings
  - • Acquired $2500 funding from multiple sources in 2007-2008
- American Institute of Aeronautics and Astronautics (AIAA), SLU Chapter
  - • **Vice-President**, March 2007 - April 2008
  - • 2008 AIAA Design, Build, Fly Competition Participant
  - • AIAA Region V Conference Planner and Volunteer

Invited Participation

- NASA Future Forum, SLU Representative, March 2008
  - • Discussed the future of NASA for the next 50 years and beyond.
- NASA INSPIRE Focus Group, Participant, August 2007
  - • Planned NASA educational events for students in grades 6 - 12.

Skills

- Platforms: Windows (Any), Apple, Linux (Any), Supercomputing Networks (Teragrid/XSEDE)
- Software: Matlab, MEEP, COMSOL, GNUPlot, Pro/Eningeer, Pro/Mechania, AutoCAD

- Languages: C/C++, Python, LaTeX, Scheme, HTML

Organizations

- American Institute of Aeronautics and Aeronautics (AIAA), 2007 - Present
- Sigma Xi, Scientific Research Society, 2009 - Present
- Institute of Electrical and Electronics Engineers (IEEE), 2011 - Present

Fields of Interest

- Nonlinear Optics, Photonics, Metamaterials, Quantum Optics, Computational Physics